A NOVEL MODEL FOR FRACTURE ACIDIZING WITH IMPORTANT THERMAL EFFECTS

A Thesis

by

JOHN BRENDAN LYONS

Submitted to the Office of Graduate and Professional Studies of
Texas A&M University
in partial fulfillment of the requirements for the degree of

MASTER OF SCIENCE

Chair of Committee,	Hisham Nasr-El-Din
Co-Chair of Committee,	Hadi Nasrabadi
Committee Member,	Mahmoud El-Halwagi
Head of Department,	Dan Hill

December 2013

Major Subject: Petroleum Engineering

ABSTRACT

Fracture acidizing is a well stimulation technique used to improve the productivity of low-permeability reservoirs, and to bypass deep formation damage. The reaction of injected acid with the rock matrix forms etched channels (that depend on injection rate, mass transport properties, formation mineralogy, reaction chemistry of the acid, and temperature) through which oil and gas can then flow upon production.

The use of a model that can effectively describe fracture acidizing is an essential step in designing an efficient and economical treatment. Several studies have been conducted on modeling fracture acidizing, however, most of these studies have not accounted for the effect of variation in acid temperature (by heat exchange with the formation and the heat generated by acid reaction with the rock) on reaction rate and mass transfer of acid inside the fracture.

In this study, a new fracture acidizing model is presented that uses the lattice Boltzmann method for fluid transport and takes into account these temperature effects. The lattice Boltzmann method incorporates both accurate hydrodynamics and reaction kinetics at the solid-liquid interface. This method is also well known for its capability to handle reactive transport in complex geometries. This enables the method to model realistic fracture shapes, on a pore-scale level, and predict the shape of the fracture after acidizing. Results of carbonate fracture dissolution with and without the thermal effects are presented. It is found that including thermal effects alters the predicted shape of the fracture after acidizing.

DEDICATION

To my loving family, girlfriend, and friends.

ACKNOWLEDGEMENTS

I am grateful for the continuous support and guidance provided by my supervisor and committee co-chair, Dr. Hadi Nasrabadi, without whom this research could not have been carried out. I would like to thank my committee chair, Dr. Hisham Nasr-El-Din, for his continuous and helpful advice. I would also like to thank Dr. Mahmoud El-Halwagi for his help and for acting as a member of my committee. Furthermore, useful advice and simulation data provided by Dr. Qinjun Kang has been greatly beneficial. Also, lengthy discussions with Ahmad Al-Douri, Mohamed Nour, Daniel Shedd, and Jeffrey Zhang have been of great benefit to my research. I would like to acknowledge the Qatar National Research Fund, NPRP 09-828-2-316, for supporting this research. The facilities and resources provided by the Harold Vance Department of Petroleum Engineering of Texas A&M University are gratefully acknowledged.

TABLE OF CONTENTS

LIST OF FIGURES

LIST OF TABLES

TABLE Page

1. INTRODUCTION

Fracture acidizing is the injection of an acid solution into a carbonate formation above the formation fracture pressure. The injected acid reacts with the fracture surface, creating etched patterns (**Fig. (1.1)**). Successful fracture acidizing is due to the uneven etching of the fracture surfaces caused by heterogeneities in the rock mineralogy and fluid leakoff. The etched patterns form channels, and thus, create lasting conductivity through the fracture. Fracture conductivity also depends on the original hardness of the formation rock and the hardness variation caused by the acid.

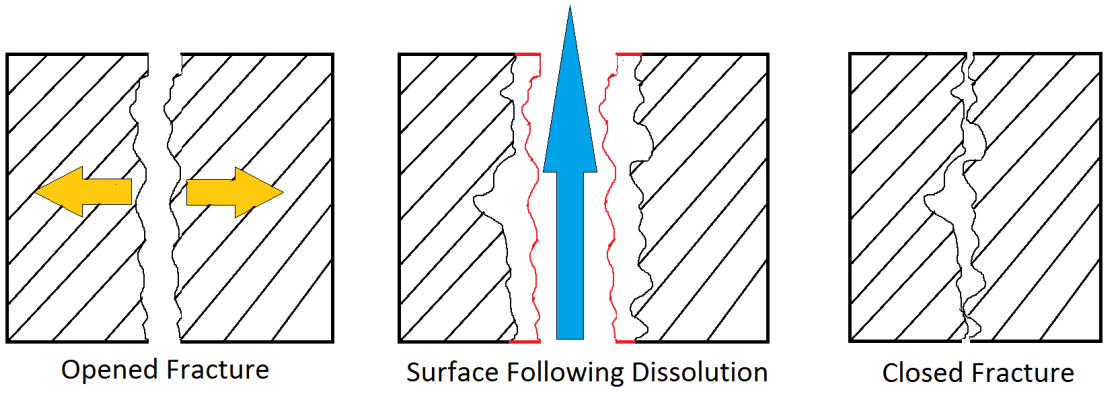

Figure 1.1: High pressure fluid forces the rock open, the acid dissolves the fracture surface, and leaves uneven etched patterns that create lasting conductivity.

Several acid systems have been used to create conductive fractures in carbonates. While the most common ones used are straight hydrochloric acid solutions (typically 15%

Reprinted with permission, throughout this thesis, from "A Novel Model for Fracture Acidizing with Important Thermal Effects" by John Lyons, Hadi Nasrabadi, and Hisham Nasr-El-Din, 2013. *SPE Canadian Unconventional Resources Conference*, 167158. Copyright 2013, Unconventional Resources Conference. Reproduced with permission of SPE.

and 28%), viscosified acid systems allow for better control of acid leak-off into the formation. One example of which is guar gel with a borate crosslinker; a time delayed gel breaker can be added to reduce the gel's viscosity, following completion of the operation.

Fracture acidizing can be used to improve the productivity of low-permeability reservoirs, and to bypass deep formation damage (**Fig. (1.2)**). An alternative technique to improve well performance is proppant fracturing.

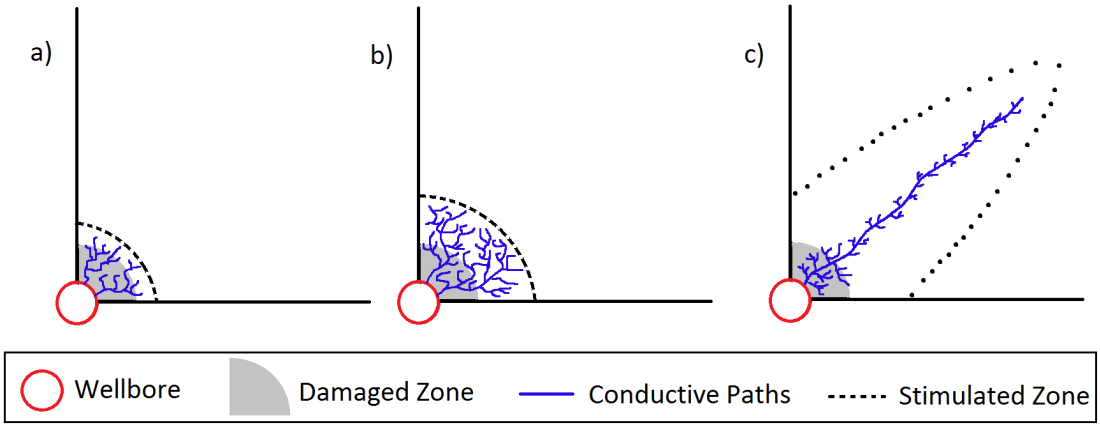

Figure 1.2: Matrix acidizing can stimulate the damaged zone (a), and sometimes bypass it (b). However, fracture acidizing can easily bypass the damage zone and produce a high conductivity pathway deep into the formation.

1.1 Proppant Fracturing vs. Fracture Acidizing

Proppant fracturing relies on injecting non-reactive fracturing fluid deep into the formation and can be carried out in both in sandstone and carbonate formations. This process results in deeper formation penetration because the fluid does not react with the fracture surface. Proppant is then pumped into the fracture, holding it open when the injection pressure decreases, and resulting in a conductive pathway.

Proppant fracturing is favored over fracture acidizing in carbonate formations when (Economides and Nolte, 2000):

1. Acid solubility is low ($<$ 65-75%)
2. The formation is relatively homogeneous
3. The acid reaction rate is low (e.g., dolomite; temperature $<$ 150 ^{o}F)
4. The formation has very low permeability (requiring a longer fracture length)
5. The formation has high closure stress (resulting in deformation of etched surfaces)
6. After contact with acid, the rock softens or creeps significantly under the fracture closure stress

Fracture acidizing is favored over proppant fracturing in carbonate formations when:

1. Acid solubility is high ($>$ 65-75%)
2. The formation is predominantly naturally fractured (complicating proppant distribution)
3. The formation exhibits porosity and permeability heterogeneities
4. The permeability is relatively high and/or near-wellbore formation damage is present
5. The formation has low closure stress (no deformation of etched surfaces)
6. After contact with acid, no softening of the rock occurs
7. The completion cannot mechanically accept proppant

1.1.1 High Acid Solubility of the Formation

For a rock-acid system where the reaction is high, a sufficient amount of rock can be dissolved and channels and wormholes can be created. This generally results in higher fracture conductivity (e.g., Nierode and Kruk (1973); Gong et al. (1998)), but not always (e.g., Antelo et al. (2009); Pournik et al. (2007)).

1.1.2 Relatively Heterogeneous Formation

In heterogeneous formations, fracture acidizing is more likely to create uneven dissolution of the fracture surface. Sufficient conductivity can, therefore, be achieved because when the fracture closes, fluid can flow through the open channels between its surfaces.

1.1.3 Low Formation Closure Stress

If the closure stress of the formation is lower than the failure stress of the rock, the etched surfaces would not collapse during closure, maintaining a constant conductivity.

1.1.4 Rock Softening

If the rock softens following acidizing, and the closure stress of the formation is higher than the failure stress of the acidized rock, the etched surfaces may collapse decreasing the conductivity.

1.2 Literature Review

Williams and Nierode (1972) developed a model that takes into account variation in the fracture geometry, acid injection rate, formation temperature, acid concentration, and rock type. They acknowledge that fracture conductivity cannot be predicted with certainty due to heterogeneity in the fracture. They note that prediction of conductivity can be improved with core samples from the formation.

Nierode and Kruk (1973) presented an evaluation of fluid loss additives and retarded acids. They also presented correlations to predict fracture conductivity based on mass of dissolved rock (ideal fracture width), assuming the walls dissolve uniformly. They conclude that measurement of fracture conductivity, by correlation or in the laboratory, would result in the lower bound of the possible conductivity, due to rock heterogeneity and acid fingering.

Using a mechanical profilometer, Ruffet et al. (1998) were able to measure the am-

plitude of acid-etched fracture surfaces as a function of flow rate and acid concentration. They found that straight acid produces etched surfaces of higher amplitude than gelled acids. They also showed that etching roughness depends on local defects in the mechanical, geometrical, or mineralogical properties of the rock.

Further studies conducted on modeling fracture acidizing (Lee and Roberts, 1980; Lo and Dean, 1989; Schechter, 1992; Settari, 1993; Settari et al., 2001), have developed correlations for predicting fracture conductivity. These have typically assumed velocity and acid distributions based on known analytical solutions.

Heat exchange with the formation, and the heat generated by the reaction of acid with the rock, can alter the reaction and diffusion rates, and mass transfer of acid within the fracture. Heat exchange can also occur between the well tubulars and the injected acid. The model presented here simulates fracture dissolution on a pore-scale level and takes into account the effect of increased fluid temperature. This model uses the lattice Boltzmann (LB) method to simulate acid transport, and reaction kinetics at the fracture surface (Kang and Lichtner, 2007). It is applicable to various homogeneous and heterogeneous reaction systems, with arbitrary geometries and with linear or non-linear kinetics. It takes into account advection, diffusion, along with continuous update of the fracture geometry.

The LB method was first introduced by McNamara and Zanetti (1988) and developed into a practical model by Higuera et al. (1989) and Higuera and Jiménez (1989). The reader is referred to Benzii and Succi (1992), Succi (2001), and Sukop and Thorne (2010) for detailed discussions on the LB method. Furthermore, it has been shown to perform well at simulating reactive transport in fractures and in complex geometries like porous media (Kang et al., 2002, 2003, 2006; Szymczak and Ladd, 2009, 2011; Verberg and Ladd, 1999). This enables the model to simulate flow in a realistic fracture geometry and to predict the shape of the fracture following acidizing. The major advantage of using the LB method is that the velocity and concentration distributions can be solved for explicitly,

in a complex geometry.

In fracture acidizing treatments, acid is injected into the formation at ambient temperature. Heat exchange occurs, by conduction, between the formation and the fluid due to the temperature difference of the two phases. Further heat exchange occurs as heat is released during the acid-rock reaction at the rock surface. Constant wall heat flux boundary conditions for the LB method have been investigated by Alazmi and Kambiz (2002).

The thermal fracture acidizing model presented here is developed using a hybrid LB technique. The approach follows that taken by Kang and Lichtner (2007), which uses the conventional LB method to simulate both the transport and reaction of fluids. This approach models the continuous dissolution of rock as acid is injected into the porous medium. As the geometry evolves, the hydrologic properties of the medium are continuously modified. The temperature distribution is updated using a finite difference (FD) approach.

Heterogeneous heat transfer (in the presence of laminar flow) in 2D domains using hybrid thermal LB FD methods has been studied in detail. Moussaoui et al. (2009) present complex flow patterns developed in the domain due to the change in location of heat source positions. In their approach, the velocities are given by the LB equations and are used to compute the energy equation. The latter is then discretized by the FD method in order to obtain the temperature field. Azwadi and Tanahashi (2008) present a study of heat transfer in a differentially heated square enclosure. This is done by discretizing the LB equations using the third-order-accurate FD upwind scheme, UTOPIA.

Jami et al. (2006) use a hybrid LB FD approach (different to the above) to study the effects of partition length, partition inclination angle, partitions number and aspect ratio cavity in an inclined enclosure. Junk (2001) presents results on the close relation of the LB method to two standard methods: relaxation schemes and explicit FD discretizations. He highlights that the discrete microscopic transport, together with weighted velocity av-

erages, is a reformulation of FD approximations and also presents a series of other comparisons between the methods. Junk and Klar (2000) show how the LB method can be reduced to a FD scheme for the incompressible Navier-Stokes equation in the low Mach number limit.

Lallemand and Luo (2003b) propose a hybrid LB method, in which the flow fields are solved by the athermal LB method, while the advection-diffusion equation for temperature is solved by a FD technique.

In this thesis, the LB and FD methods are introduced. This is followed by a description of the process of fracture dissolution, heat generation and reaction rate variation. The process of conversion from physical to lattice units is then described. Validation of the reactive transport model is then given. Finally, results of the thermal fracture acidizing model are presented. In the equations that follow, bold letters represent vectors, unless otherwise stated.

2. LATTICE BOLTZMANN MODEL BACKGROUND

2.1 Lattice Gas Automata

The lattice gas automata method (a precursor to the LB method) is one which attempts to recover macroscopic fluid dynamics (e.g., Navier-Stokes equations) using microscopic physical principles. The lattice is a grid, where sites take a certain number of different states. In lattice gas, the various states are particles with given velocities. At each time step, a particle moves based on its velocity. Two processes are then carried out: i) propagation and ii) collision (where necessary). The simplest LGA is the HPP model.

2.1.1 HPP Model

The HPP (Hardy, Pomeau, and de Pazzis) model (Hardy et al., 1973) has a 2D square grid such that each node has four neighbors. The possible velocities of each particle are: $\mathbf{c}_1 = (1,0)$, $\mathbf{c}_2 = (0,1)$, $\mathbf{c}_3 = (-1,0)$. $\mathbf{c}_4 = (0,-1)$ (**Fig. (2.1)**). At each time step, the particles move one lattice unit in the direction of their velocity (**Fig. (2.2)**).

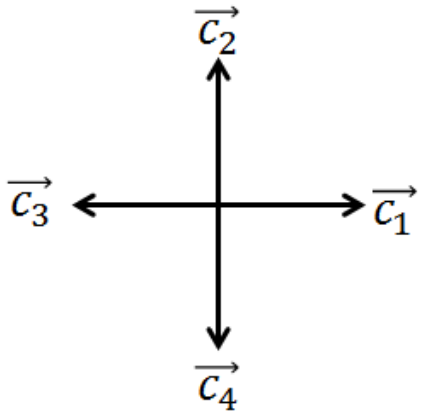

Figure 2.1: The possible velocity vectors for the HPP model.

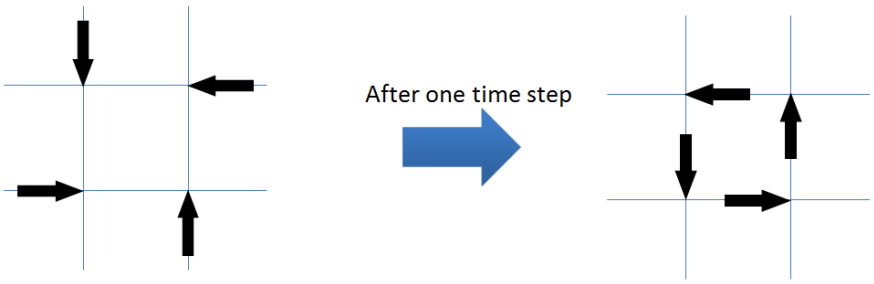

Figure 2.2: Four particles move from one lattice node to the next, after one time step.

If two or more particles meet at a given lattice node after a time step, a collision occurs. In order to conserve mass and momentum, the number of particles and the total velocity must be equal before and after the collision. For example, if two particles collide head-on their final velocities are at right-angles to their initial velocities (**Fig. (2.3)**), i.e., in both cases the sum of their velocities is zero and so momentum is conserved.

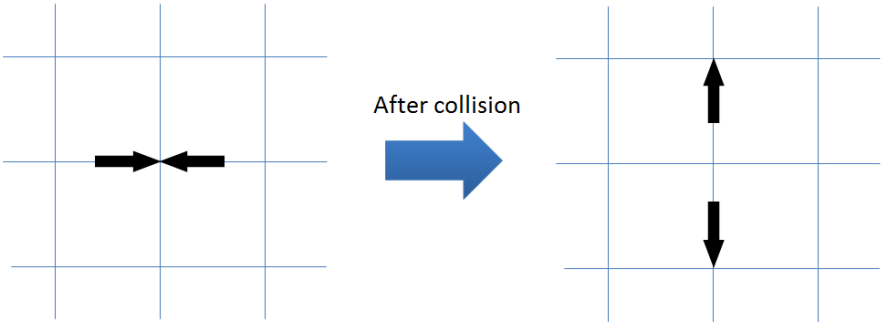

Figure 2.3: The particles bounce back, elastically, after a head-on collision.

The parameters used in the simulation are related to the physical parameters through the lattice spacing, Δx, and the lattice time, Δt. For example, the physical particle velocity can be converted to lattice velocity by:

$$\mathbf{c}_{i,\text{physical}} = \frac{\Delta x}{\Delta t}\mathbf{c}_{i,\text{lattice}} \ . \tag{2.1}$$

The particle density at each lattice site can be calculated by:

$$\rho(\mathbf{x},t) = \sum_i n_i(\mathbf{x},t) \ , \tag{2.2}$$

where $\rho(\mathbf{x},t)$ is the particle density at a given node with position $\mathbf{x}$, at time t, and n_i is the Boolean occupation number, i.e., the number of particles present (0 or 1) at the node.

The total momentum at each lattice site can be calculated by:

$$\rho(\mathbf{x},t)\mathbf{u}(\mathbf{x},t) = \sum_i \mathbf{c}_i n_i(\mathbf{x},t) \ . \tag{2.3}$$

2.1.2 FHP Model

The FHP (Frisch, Hasslacher, and Pomeau) model was shown to recover the incompressible Navier-Stokes equations (Frisch et al., 1986). This was achieved by using a hexagonal lattice instead of a square one, thus providing extra rational invariance. The possible velocities of each particle are: $\mathbf{c}_1 = (1,0)$, $\mathbf{c}_2 = (1/2,\sqrt{3}/2)$, $\mathbf{c}_3 = (-1/2,\sqrt{3}/2)$, $\mathbf{c}_4 = (-1,0)$, $\mathbf{c}_5 = (-1/2,-\sqrt{3}/2)$, $\mathbf{c}_6 = (1/2,-\sqrt{3}/2)$ (**Fig. (2.4)**).

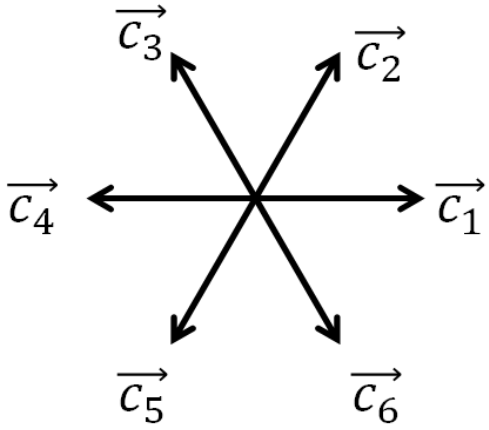

Figure 2.4: The possible velocity vectors for the HPP model.

The FHP model allows for two outcomes of head-on collision, each with equal probability (**Fig. (2.5)**). In order to recover the incompressible Navier-Stokes equations, the viscosity must be given by:

$$\nu = \frac{\Delta x^2}{\Delta t}\left(\frac{1}{2\rho_0(1-\rho_0/6)^3} - \frac{1}{8}\right) . \tag{2.4}$$

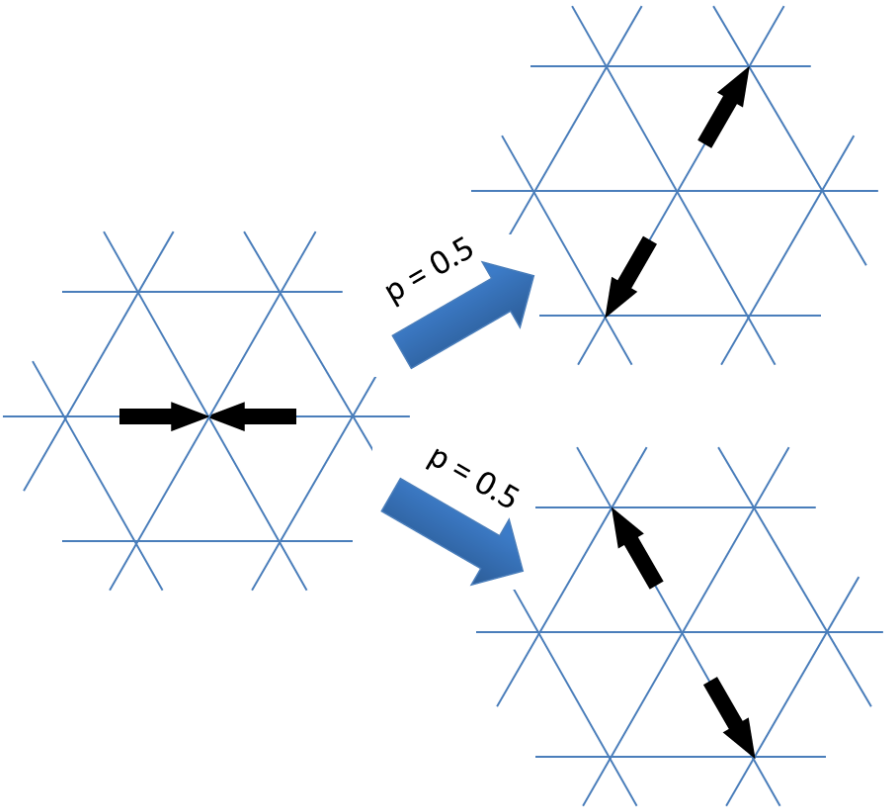

Figure 2.5: The particles have a 50% chance of propagating in either of two perpendicular directions, after a head-on collision.

2.1.3 LB Model

The LB model is inspired by the above models. In 2D, it can have a 7-, 9-, or 13-speed lattice, although 9 is the most common. Also, instead of having single particles at each lattice site, a probability density distribution of particles, $f_i(\mathbf{x},t)$, is defined. The particle density at each lattice site can then be calculated by:

$$\rho(\mathbf{x},t) = \sum_i f_i(\mathbf{x},t) \ , \tag{2.5}$$

and the total momentum at each lattice site can be calculated by:

$$\rho(\mathbf{x},t)\mathbf{u}(\mathbf{x},t) = \sum_i \mathbf{c}_i f_i(\mathbf{x},t) \ . \tag{2.6}$$

Also, the collision of particles is described by a collision operator based on an equilibrium distribution and a relaxation time. The following section describes this method in more detail.

3. MODELING REACTIVE TRANSPORT

3.1 LB Method: Fluid Velocity Update

The benefit of using the LB method to model reactive transport is that it takes into account the explicit topography of the pore space and that the transport coefficients (viscosity, diffusivity, and reaction rate) are all determined independently, so there are no fitting parameters. The state of the LB system is described by a discretized probability density function, $f_i(\mathbf{x},t)$, which describes the number of particles positioned at a lattice node $\mathbf{x}$, at time t and with velocity $\mathbf{c}_i$. In this study, the lattice is square and the space and time intervals, Δx and Δt, respectively, are unity (implying that the lattice velocity, $c = \Delta x/\Delta t = 1$). The LB velocity evolution equation is then:

$$f_i(\mathbf{x}+\mathbf{c}_i\Delta t, t+\Delta t) - f_i(\mathbf{x},t) = -\frac{f_i(\mathbf{x},t) - f_i^{\mathrm{eq}}(\rho,\mathbf{u})}{\tau} \; . \tag{3.1}$$

The relaxation time, τ, is related to the kinematic viscosity by $\nu = (\tau - 0.5)/3$. For the D2Q9 (2 dimensional, 9-speed) LB model, the equilibrium distribution, f_i^{eq}, is given by:

$$f_i^{\mathrm{eq}} = \omega_i \rho \left[1 + \frac{3\mathbf{c}_i \cdot \mathbf{u}}{c^2} + \frac{9(\mathbf{c}_i \cdot \mathbf{u})^2}{2c^4} - \frac{3\mathbf{u}^2}{2c^2} \right], \tag{3.2}$$

where ρ and $\mathbf{u}$ are the fluid density and velocity, respectively. The weight coefficients are $\omega_0 = 4/9$, $\omega_i = 1/9$ for $i = 1,2,3,4$ and $\omega_i = 1/36$ for $i = 5,6,7,8$. The velocity vectors, $\mathbf{c}_i$, are given by:

$$\mathbf{c}_i = \begin{cases} 0, & \text{if } i = 0, \\ \left(\cos\frac{(i-1)\pi}{2}, \sin\frac{(i-1)\pi}{2}\right) c, & \text{if } i = 1,\ldots,4, \\ \sqrt{2}\,(\cos[\,\frac{(i-5)\pi}{2} + \frac{\pi}{4}\,], \sin[\,\frac{(i-5)\pi}{2} + \frac{\pi}{4}\,])\, c, & \text{if } i = 5,\ldots,8\;. \end{cases} \tag{3.3}$$

The mass and momentum densities are then calculated by:

$$\rho(\mathbf{x},t) = \sum_i f_i(\mathbf{x},t) \ , \tag{3.4}$$

$$\rho(\mathbf{x},t)\mathbf{u}(\mathbf{x},t) = \sum_i \mathbf{c}_i f_i(\mathbf{x},t) \ . \tag{3.5}$$

As is well known, Eqs. (3.4) and (3.5) can be used to recover the correct continuity and Navier-Stokes equations using the Chapman-Enskog expansion (Chen et al., 1992) :

$$\frac{\partial \rho}{\partial t} + \nabla \cdot (\rho \mathbf{u}) = 0 \ , \tag{3.6}$$

$$\rho \left[\frac{\partial \mathbf{u}}{\partial t} + (\mathbf{u} \cdot \nabla)\mathbf{u} \right] = -\nabla \rho + \nabla \cdot [\rho \nu (\nabla \mathbf{u} + \mathbf{u} \nabla] \ , \tag{3.7}$$

where $p = \rho RT$ is the fluid pressure, and R, T, and ν are the universal gas constant, absolute temperature, and kinematic viscosity, respectively.

3.2 LB Method: Solute Concentration Update

Solute (acid) transport is also modeled using the LB method to solve the convection-diffusion equation. It is assumed that solute concentrations are sufficiently low not to influence the solvent flow. The acid concentration evolution can then be described by the following LB equation:

$$g_i(\mathbf{x} + \mathbf{c}_i \Delta t, t + \Delta t) - g_i(\mathbf{x},t) = -\frac{g_i(\mathbf{x},t) - g_i^{\mathrm{eq}}(C,\mathbf{u})}{\tau_{\mathrm{aq}}} + \omega_i q_s \ . \tag{3.8}$$

The relaxation time, τ_{aq}, is related to the diffusion coefficient by $\mathcal{D} = (\tau_{\mathrm{aq}} - 0.5)/2$ and q_s is the source term for chemical reaction in the bulk fluid (and is neglected here). C is the solute concentration and the equilibrium distribution, g_i^{eq}, is given by (Noble, 1997):

$$g_i^{\mathrm{eq}} = \frac{C}{4} + \frac{C(\mathbf{c}_i \cdot \mathbf{u})}{2c^2} \ , \tag{3.9}$$

where the weight coefficients are $\omega_i = 1/4$ for $i = 1,2,3,4$. For the D2Q4 (2 dimensional, 4-speed) LB model:

$$\mathbf{c}_i = \left(\cos\frac{(i-1)\pi}{2}, \sin\frac{(i-1)\pi}{2}\right) c, \quad i = 1,\ldots,4\ . \tag{3.10}$$

The solute concentration is then calculated by:

$$C(\mathbf{x},t) = \sum_{i=1}^{4} g_i(\mathbf{x},t)\ . \tag{3.11}$$

Using Eq. (3.11) and the Chapman-Enskog expansion, the correct convection-diffusion-reaction equation can be recovered (Dawson et al., 1993):

$$\frac{\partial C}{\partial t} + (\mathbf{u}\cdot\nabla)C = \nabla\cdot(\mathcal{D}\nabla C) + q_s\ . \tag{3.12}$$

For more details the reader is referred to Lichtner and Kang (2007), Appendix A.

3.2.1 Multi-Component Planar Boundary Condition

If it is assumed that the concentrations of the aqueous species are sufficiently low such that their effect on the solution velocity and density are negligible, then the reactive transport of the solute species can be described by a separate set of distributions, g_i (i.e., the convection-diffusion and Navier-Stokes equations are uncoupled). g_i can be given in terms of its equilibrium and non-equilibrium parts, for the j$^{\text{th}}$ component:

$$g_{i,j} = g_{i,j}^{eq} + g_{i,j}^{neq}\ . \tag{3.13}$$

By choosing appropriate values for $\mathbf{e}_i$ and thus $g_{i,j}^{eq}$, the pore-scale advection-diffusion equation for Ψ_j can be recovered (Dawson et al., 1993):

$$\frac{\partial \Psi_j}{\partial t} + \nabla\cdot\Omega_j = 0\ , \tag{3.14}$$

where

$$\Psi_j = \sum_i g_{i,j}, \tag{3.15}$$

is the zeroth order velocity moment and

$$\Omega_j = \mathbf{u}\Psi_j - \mathcal{D}\nabla\Psi_j \ , \tag{3.16}$$

is the flux of the total concentration of the j^{th} primary species due to advection and diffusion.

The boundary condition for the total concentration, Ψ_j, is given by:

$$\mathcal{D}\frac{\partial\Psi_j}{\partial n} = \sum_{m=1}^{N_m} \nu_{j,m} I_m^* \ , \tag{3.17}$$

where n is the directional normal into the fluid at the solid-fluid interface, $\nu_{j,m}$ are the stoichiometric coefficients, I_m^* is the reaction rate for m^{th} mineral reaction at the mineral interface and is given by:

$$I_m^* = -k_m(1 - K_m Q_m), \tag{3.18}$$

where k_m is the reaction rate constant, K_m is the equilibrium constant, and Q_n is the ion activity product, given by:

$$Q_m = \prod_{j=1}^{N_C} \left(\gamma_j C_j\right)^{\nu_{j,m}} \ . \tag{3.19}$$

In order to determine concentration boundary condition, the first order velocity moment is required. The following relation is proposed by (Noble, 1997), for the D2Q4 lattice:

$$\sum_i g_{i,j}\mathbf{e}_i = \Psi_j \mathbf{u} - \frac{\tau(\delta x)^2}{2\delta t}\nabla\Psi_j \ . \tag{3.20}$$

It should be noted that the lattice diffusivity is lower for the D2Q4 than it is for the D2Q9 lattice:

$$\mathcal{D} = \frac{\tau_{aq}(\delta x)^2}{3\delta t} \ . \tag{3.21}$$

The concentration boundary condition can then be expressed as:

$$\sum_i g_{i,j}\mathbf{e}_i = \Psi_j \mathbf{u} - \mathcal{D}\nabla\Psi_j = \Omega_j \ . \tag{3.22}$$

when $\mathbf{u}$ is assumed to be zero at the boundary then at boundary shown in Fig. (3.1):

$$g_{2,j} - g_{4,j} = -\frac{\mathcal{D}}{c}\frac{\partial\Psi_j}{\partial y} = \frac{1}{c}\sum_{m=1}^{N_m} \nu_{j,m} k_m (1 - K_m Q_m) \ . \tag{3.23}$$

At a stationary wall, the non-equilibrium part of the distribution function is proportional to the dot product of its microscopic velocity and the concentration gradient (He et al., 2000). As a result, the non-equilibrium parts can be set equal but with opposite signs, for example:

$$g_{2,j}^{neq} = -g_{4,j}^{neq} \ , \tag{3.24}$$

which implies that:

$$\begin{aligned} g_{2,j} + g_{4,j} &= g_{2,j}^{eq} + g_{4,j}^{eq} \\ g_{2,j} + g_{4,j} &= \frac{1}{2}\Psi_j \ . \end{aligned} \tag{3.25}$$

3.2.2 Single-Component Planar Boundary Condition

Applying Eqs. (3.23) and (3.25) to a single-aqueous-component ($j = 1$) single mineral reaction, where $N_C = N_m = \nu_{11} = \gamma = 1$ and $N_R = 0$, such that $\Psi_1 = Q_1 = C$, $k_1 = k$, and

$K_1 = K$. In order to determine concentration boundary condition at the fracture surface, the first order velocity moment is required. The following relation is proposed by Noble (1997), for the D2Q4 lattice and a single-aqueous-component single mineral reaction:

$$\sum_i g_i \mathbf{c}_i = C\mathbf{u} - \mathcal{D}\nabla C \ . \tag{3.26}$$

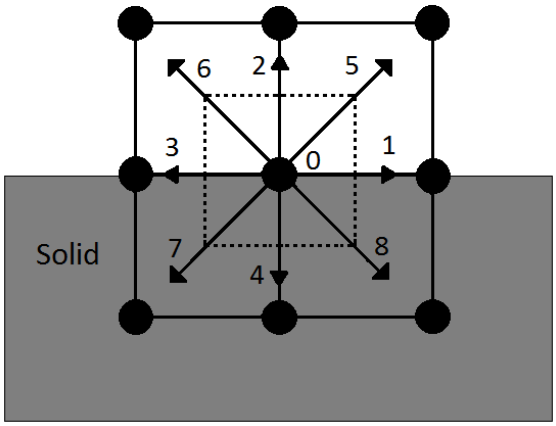

Figure 3.1: Planar boundary node distributions for both D2Q4 and D2Q9 lattices.

Expanding the summation and assuming **u** to be zero at the boundary **(Fig. (3.1))**, the concentration boundary condition can then be expressed as:

$$g_2 - g_4 = -\frac{1}{c}\mathcal{D}\nabla C = \frac{1}{c}k(1 - KC) \ . \tag{3.27}$$

At a stationary wall, the non-equilibrium part of the distribution function is proportional to the dot product of its microscopic velocity and the concentration gradient. As a result, the non-equilibrium parts can be set equal but with opposite signs (He et al., 2000), for example:

$$g_2^{neq} = -g_4^{neq} \,, \tag{3.28}$$

which implies that:

$$\begin{aligned} g_2 + g_4 &= g_2^{eq} + g_4^{eq} \\ &= \frac{1}{2}C \,. \end{aligned} \tag{3.29}$$

Combining Eqs. (3.27) and (3.29), the following boundary condition is obtained:

$$\begin{aligned} \left(\frac{C}{2} - g_4\right) - g_4 &= k(1 - KC) \,, \\ 2g_4 &= C(\frac{1}{2} + kK) - k \,, \\ C &= \frac{2g_4 + k}{kK + \frac{1}{2}} \,, \\ C &= \frac{2g_4 + k_r C_{\text{eq}}}{k_r + \frac{1}{2}} \,, \end{aligned} \tag{3.30}$$

where k is the reaction rate constant, K is the equilibrium constant, $k_r = kK$ and $C_{\text{eq}} = 1/K$.

3.2.2.1 Large Equilibrium Constant Limit

In the limit of a large equilibrium constant, $K \to \infty$, the dissolution rate of solute becomes:

$$\begin{aligned} r_D &= k(KC - 1) \\ &= k\left(K\frac{2g_4 + k_r C_s}{k_r + \frac{1}{2}} - 1\right) \\ &= k\left(\frac{2g_4 + k}{k + \frac{1}{2K}} - 1\right) \\ &\to k\left(\frac{2g_4 + k}{k} - 1\right), \quad \text{as } K \to \infty \\ &= 2g_4 \end{aligned} \tag{3.31}$$

4. FLUID TEMPERATURE UPDATE

Mezrhab et al. (2004) propose that to simulate fluid flows that are weakly coupled to temperature (or other quantity) in a convective situation, the athermal LB method can be used, followed by a FD scheme to determine the temperature field. At each time step the results of each computation can then be used to determine perturbations of the temperature (or other quantity).

The hybrid LB FD method has also been shown to demonstrate radiation and natural convection in a cylinder (Mezrhab et al., 2008). The LB FD method has also been used to model reactive flow in rock fractures (Kim et al., 2003) based on experimental results (Durham et al., 2001).

In order to determine the effect of temperature on wormhole formation within a fracture, the temperature distribution should be calculated while the reactant propagates through the fracture. Given the fluid velocity, u, the temperature can be determined by solving for T in the advection-diffusion equation (Lallemand and Luo, 2003a,b):

$$\partial_t T = -u \cdot \nabla T + \kappa \Delta T + q_2(\gamma - 1) c_{s_0}^2 \nabla \cdot u \,, \tag{4.1}$$

where κ is the fluid thermal diffusivity (assumed to be constant in time and space), $q_2 = 1$, γ is the specific heat ratio and c_{s_0} is the isothermal speed of sound.

This approach is used to model acoustic phenomena (with linear compressibility). However, this study does not consider compressibility, i.e., $\nabla \cdot u = 0$ similar to Mezrhab et al. (2004). Thus, the temperature field can be determined by:

$$\partial_t T = -u \cdot \nabla T + \kappa \Delta T \,. \tag{4.2}$$

Lallemand and Luo's FD treatment of the temperature field is as follows:

$$\partial_x^* f(i,j) = f(i+1,j) - f(i-1,j) - 1/4[(f(i+1,j+1) - f(i-1,j+1) + f(i+1,j-1) - f(i-1,j-1))] , \quad (4.3)$$

$$\partial_y^* f(i,j) = f(i,j+1) - f(i,j-1) - 1/4[(f(i+1,j+1) - f(i+1,j-1) + f(i-1,j+1) - f(i-1,j-1))] \text{ and} \quad (4.4)$$

$$\Delta^* f(i,j) = 2[f(i+1,j) + f(i-1,j) + f(i,j+1) + f(i,j-1)] - 1/2[(f(i+1,j+1) + f(i-1,j+1) + f(i-1,j-1) , + f(i+1,j-1))] - 6f(i,j), \quad (4.5)$$

where * denotes the equivalent FD operation and f is an arbitrary function (separate to the probability density function, f_i). Written out fully and factorized the update equation for T is then:

$$\begin{aligned} T_{i,j}^{k+1} &= (-u_x q + 2r)T_{i+1,j}^k + (u_x q + 2r)T_{i-1,j}^k + (-u_y q + 2r)T_{i,j+1}^k \\ &+ (u_y q + 2r)T_{i,j-1}^k + (0.25q[u_x + u_y] - 0.5r)T_{i+1,j+1}^k + (0.25q[-u_x + u_y] - 0.5r)T_{i-1,j+1}^k \\ &+ (-0.25q[u_x + u_y] - 0.5r)T_{i-1,j-1}^k + (0.25q[u_x - u_y] - 0.5r)T_{i+1,j-1}^k + (1 - 6r)T_{i,j}^k \end{aligned} \quad (4.6)$$

Alternatively, the standard 2D FD discretization takes the form (the superscript and subscript denote temporal and spatial indices, respectively):

$$\partial_t T = \frac{T_{i,j}^{k+1} - T_{i,j}^k}{\Delta t}, \quad (4.7)$$

$$u \cdot \nabla T = u_{x_{i,j}} \cdot \frac{T_{i+1,j}^k - T_{i,j}^k}{\Delta x} + u_{y_{i,j}} \cdot \frac{T_{i,j+1}^k - T_{i,j}^k}{\Delta y}, \quad (4.8)$$

$$\Delta T = \frac{T_{i+1,j}^k - 2T_{i,j}^k + T_{i-1,j}^k}{\delta x^2} + \frac{T_{i,j+1}^k - 2T_{i,j}^k + T_{i,j-1}^k}{\Delta y^2} \text{ and} \quad (4.9)$$

$$\nabla \cdot u = \frac{u^k_{x_{i+1,j}} - u^k_{x_{i,j}}}{\Delta x} + \frac{u^k_{x_{i,j+1}} - u^k_{x_{i,j}}}{\Delta y} \tag{4.10}$$

where Δx, Δy are spatial discretizations and Δt is the time discretization, and are equivalent to those used in the LB model.

Both approaches of FD update have been implemented, along with an implicit formulation (given in Appendix A). However, the standard FD update has proven more stable and requires less computational effort.

4.1 Fracture Dissolution and Heat Generation

The overall rate of acid consumption or mineral dissolution depends on two separate phenomena: the rate of transport of acid to the mineral surface by diffusion or convection and the actual reaction rate on the mineral surface. In general, one of these processes is much faster than the other and, thus, the faster process can be ignored (because it is assumed to occur in an insignificant amount of time relative to the slower process).

For example, the HCl-$CaCO_3$ surface-reaction rate is high relative to the rate of acid transport to the surface and so its overall reaction rate is governed by the latter process. Calcite is the salt of a weak acid and so will dissolve in any strong acid:

$$CaCO_3(s) + 2\,H^{++} \rightleftharpoons Ca^{++} + CO_2(aq) + H_2O$$

In the case of HCl (a strong acid) the reaction may be considered to be irreversible. Lund et al. (1975) carried out measurements of the HCl-$CaCO_3$ reaction rate. Their experiments were performed with temperatures ranging from -15.6 to 25^{o}C and 800 psig. The reaction rate for HCl-$CaCO_3$ was measured to be:

$$-r_{\mathrm{HCl}} = E_f C^{\alpha}_{\mathrm{HCl}} \,, \tag{4.11}$$

where

$$E_f = E_f^0 \exp\left(-\frac{\Delta E}{RT}\right) , \tag{4.12}$$

where α is the order of the reaction (a measure of how strongly the reaction rate depends on the concentration of the acid), C_{HCl} is the concentration of HCl (in g-mol/liter), and ΔE is the activation energy for the surface reaction (in kcal/g-mol). These constants are listed in **Table 4.1.**

Table 4.1: Reaction constants in HCl-$CaCO_3$ reaction (Economides and Nolte, 2000).

α	E_f^0	$\frac{\Delta E}{R}$
0.63	7.291×10^7	7.551×10^3

Calcite-hydrochloric acid reactions have also been carried out at higher pressures to simulate reservoir conditions, e.g., (Barron et al., 1962; Nierode and Williams, 1971). In this model it is assumed that the reaction rate constant is unaffected by the concentration of reactants or products.

The reaction rate of HCl with dolomite can also be described by Eq. (4.11) (Lund et al., 1973). The constants are listed in **Table 4.2**.

Table 4.2: Constants in HCl-dolomite reaction (Economides and Nolte, 2000).

α	E_f^0	$\frac{\Delta E}{R}$
$\frac{6.18\times10^{-4}T}{1-2\times10^{-3}T}$	$\frac{9.4\times10^{11}}{1000^{\alpha}}$	11.32×10^3

In particular the reaction rates were found to be:

$$\begin{aligned} -r_{HCl} &= 2.6 \times 10^{-6} C_{HCl}^{0.44} \quad \text{at } 25^{o}\text{C and} \\ -r_{HCl} &= 6.6 \times 10^{-5} C_{HCl}^{0.61} \quad \text{at } 50^{o}\text{C and} \\ -r_{HCl} &= 5.4 \times 10^{-3} C_{HCl}^{0.83} \quad \text{at } 100^{o}\text{C.} \end{aligned} \tag{4.13}$$

At room temperature it was found that, at the solid-liquid interface, calcite reacts approximately 650 times faster than dolomite.

The effect of temperature on reaction rate for the HCl-$CaCO_3$ reaction is shown in **Fig. (4.1)** based on Eq. (4.11) and Table 4.1 (Lund et al., 1975). A linear relationship between concentration and reaction rate is observed while a non-linear one is observed when varying the temperature.

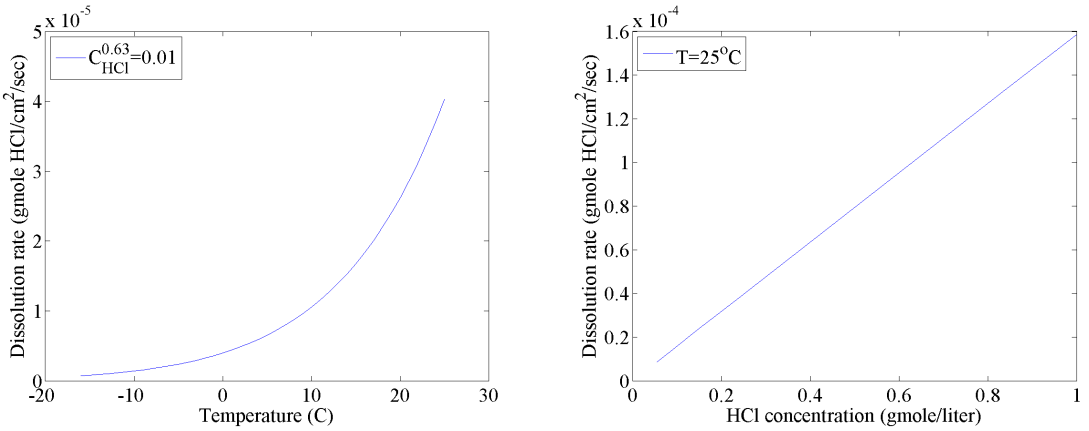

(a) (b)

Figure 4.1: HCl-$CaCO_3$ reaction rate as a function of a) temperature and b) HCl concentration.

The effect of temperature on reaction rate for the HCl-$CaMg(CO_3)_2$ reaction is shown in **Fig. (4.2)** based on Eq. (4.11) and Table 4.2 (Lund et al., 1973). A linear relationship between concentration and reaction rate is observed while a non-linear one is observed when varying the temperature. The temperature and concentration ranges for both figures are similar to those from the original experiments. Reaction rates with formic acid are given in Appendix B.

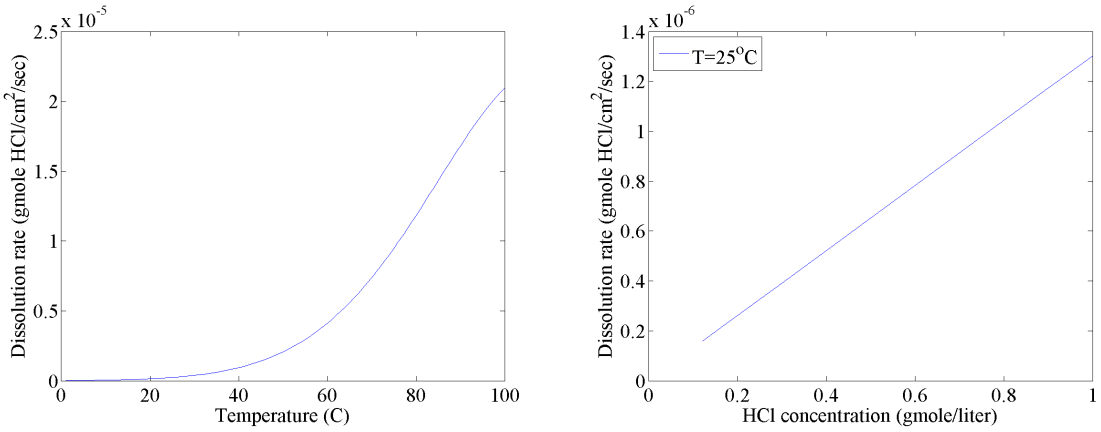

(a) (b)

Figure 4.2: HCl-$CaMg(CO_3)_2$ reaction rate as a function of a) temperature and b) HCl concentration.

Lund et al. (1973) states "Since the range of temperatures in most oil wells is approximately $50 - 150$ °C one would expect the acidization of dolomite formations to be reaction controlled at the lower temperatures (50 °C) and diffusion controlled at the higher temperatures (150 °C)."

The rate of dissolution of HCl can be determined assuming a first-order heterogeneous reaction:

$$r_{\mathrm{HCl}} = \mathcal{D}\frac{\partial C}{\partial n} = -k(1-KC) \ , \tag{4.14}$$

where $\mathcal{D}$ and C are the diffusion coefficient and concentration of aqueous HCl, respectively, and n is the surface normal pointing into the fluid.

4.2 Rock Dissolution: VOP method

The volume of pixel (VOP) method (Chen et al., 2013; Lichtner and Kang, 2007) is adopted to model the rock dissolution. In this method, each pixel (node) is assigned a value representing the volume of the rock. In physical units, the dimensionless volume of the rock node, ϕ, is updated by:

$$\frac{\partial \phi}{\partial t} = -V_m \nu_s k a (1-KC) \ , \tag{4.15}$$

where V_m is the mineral molar volume, ν_s is the stoichiometric number, and $a = 1/\Delta x^2$ is the specific surface area. ϕ is given an initial value of unity. In its discrete form, Eq. (5.22) can be written as:

$$\phi(t+\Delta t) = \phi(t) - V_m \nu_s a k (1-KC)\Delta t \ . \tag{4.16}$$

Heat is generated as a function of rock dissolution. The volume of rock dissolved per time step is given by:

$$V_{\mathrm{diss}} = \frac{\partial \phi}{\partial t} \ , \tag{4.17}$$

and thus the mass dissolved per rock node is:

$$m_{\mathrm{rock}} = \frac{\rho_{\mathrm{rock}}}{V_{\mathrm{diss}}} \ , \tag{4.18}$$

where ρ_{rock} is the rock density. Heat is released into the fluid node normal to the face of

the rock node that has dissolved. The specific heat capacity is used to update the fluid temperature:

$$\Delta Q = c_p m_{\text{rock}} \Delta T \ , \tag{4.19}$$

where c_p is the specific heat capacity.

4.3 Reaction Rate Variation with Temperature

As injected acid reaches the fracture surface, an exothermic reaction occurs increasing the surrounding acid temperature. The reaction rate at an arbitrary temperature, T, can be calculated using the Arrhenius equation:

$$k_{r,T} = k_{r,T_0} \exp\left(-\frac{\Delta E}{R}\left(\frac{1}{T} - \frac{1}{T_0}\right)\right) \ . \tag{4.20}$$

5. LB PARAMETER ANALYSIS

5.1 Conversion from Physical Units to Lattice Units

The conversion factor, C_H, from the physical height and the height in lattice units (lu) is given by:

$$C_H = H/\tilde{H} \ , \tag{5.1}$$

where H is the fracture characteristic height, $\tilde{H}$ is the lattice resolution. The tilde, $\tilde{}$, denotes the lattice quantity. In order to calculate the lattice time (lt) step, the viscosity conversion factor is rearranged:

$$\begin{aligned} [\nu] &= \frac{[m^2]}{[s]} \\ &= \frac{C_H^2}{C_t} \ , \end{aligned} \tag{5.2}$$

and

$$\nu = \tilde{\nu} \times C_\nu \ , \tag{5.3}$$

where ν and $\tilde{\nu}$ are the physical and lattice fluid viscosities, respectively. This implies that:

$$\nu = \tilde{\nu} \frac{C_H^2}{C_t} \ , \tag{5.4}$$

and thus:

$$
\begin{aligned}
C_t &= \frac{\tilde{\nu}}{\nu}\left(\frac{H}{\tilde{H}}\right)^2 \\
&= C_H^2\frac{\tilde{\nu}}{\nu}\,.
\end{aligned}
\tag{5.5}
$$

If the physical Péclet number is assumed to be equal the Péclet number on the lattice, i.e., $Pe = \tilde{P}e = \tilde{u}\tilde{H}/\tilde{\mathcal{D}}$ then the lattice velocity can be determined by:

$$
\tilde{u} = \frac{\tilde{\mathcal{D}}}{\tilde{H}}Pe\,. \tag{5.6}
$$

Similarly, if the physical Damköhler number is assumed to be equal the Damköhler number on the lattice, i.e., $Da = \tilde{D}a = \tilde{k}\tilde{H}/\tilde{\mathcal{D}}$ then the lattice reaction rate can be determined by:

$$
\tilde{k_r} = \frac{\tilde{\mathcal{D}}}{\tilde{H}}Da\,. \tag{5.7}
$$

For example, considering uniform flow ($u = 3$ cm/s) through a fracture of height 0.2 cm with reaction rate $k_r = 0.1$ cm/s and solute diffusion coefficient, $\mathcal{D} = 1\times10^{-4}$ cm^2/s, **Table 5.1** gives the lattice parameters.

From the above example, the following can be concluded:

$$
\begin{aligned}
C_H &= \frac{H}{\tilde{H}} \\
&= 2\times10^{-5}\ \text{m}\,,
\end{aligned}
\tag{5.8}
$$

and

Table 5.1: Conversion from physical to lattice units.

Physical units		Lattice units
H	2×10^{-3} m	100
ν	1×10^{-6} m^2 s^{-1}	$\frac{1}{6}$
u	0.03 m s^{-1}	0.1
τ_ν		1
$\mathcal{D}$	1×10^{-8} m^2 s$^-1$	$\frac{1}{6}$
k_r	1×10^{-3} m s^{-1}	$\frac{1}{3}$
$\tau_\mathcal{D}$		1

$$\begin{aligned} C_t &= \frac{\tilde{\nu}}{\nu}\left(\frac{H}{\tilde{H}}\right)^2 \\ &= 6.67 \times 10^{-5} \text{ s} . \end{aligned} \tag{5.9}$$

Thus to simulate 1 second of flow through this fracture requires 15,000 time steps. For stability reasons, the LB method requires the lattice velocity to be less than 0.1 lu/lt. It should be noted that the reaction rate and solute diffusion coefficient can, equivalently, be calculated by:

$$\tilde{k}_r = k_r \frac{C_t}{C_H} , \tag{5.10}$$

and

$$\tilde{\mathcal{D}} = \mathcal{D} \frac{C_t}{C_H^2} . \tag{5.11}$$

If the concentration, C, is given in mol/L and the equilibrium constant, K, is given in L/mol, then the lattice concentrations do not need to be converted because the dissolution

update equation, Eq. (4.14), contains the dimensionless term KC.

5.2 Dimensional Analysis: Reaction Rate

The reaction rate for the first order reaction, $A_{(aq)} \rightleftharpoons A_{(s)}$ can be expressed as:

$$I = k_f C - k_b = k_f \left(C - \frac{k_b}{k_f} \right) , \tag{5.12}$$

where C, k_f and k_b are the reactant concentration, forward, and backward reaction rate constants, respectively. The reaction rate can also be written as:

$$I = k_r (C - C_{eq}) . \tag{5.13}$$

Comparing the above equations gives:

$$k_r = k_f , \quad C_{eq} = \frac{k_b}{k_f} . \tag{5.14}$$

Furthermore, Eq. (5.12) can be rewritten as:

$$I = k_f C - k_b = -k_b \left(1 - \frac{k_f}{k_b} C \right) . \tag{5.15}$$

In Kang and Lichtner (2007), the rate is expressed as:

$$I = -k_m (1 - K_m Q_m) , \tag{5.16}$$

for a single component aqueous solution, $m = 1$ and $Q_m = C$. Again, comparing the above two equations gives:

$$k_m = k_b , \quad K_m = \frac{1}{C_{eq}} = \frac{k_f}{k_b} . \tag{5.17}$$

The dimensions of the above terms are:

$$[k_r] = [k_f] = \frac{L}{T} , \tag{5.18}$$

$$[k_m] = [k_b] = \frac{M}{L^2 T} \ , \tag{5.19}$$

$$[C] = \frac{M}{L^3} \ \text{ and} \tag{5.20}$$

$$[K_m] = \left[\frac{1}{C_{eq}}\right] = \frac{L^3}{M} \ . \tag{5.21}$$

where M, L and T are mass, length, and time, respectively.

5.3 Dimensional Analysis: Dissolution Rate

The volume of pixel method (VOP) (Chen et al., 2013; Lichtner and Kang, 2007) is adopted to model the rock dissolution. In physical units, the dimensionless volume of the rock node, ϕ, is updated by:

$$\frac{\partial \phi}{\partial t} = -V_m k a (1 - K C_{aq}) \ , \tag{5.22}$$

where V_m is the mineral molar volume and a is the specific surface area, and has dimension:

$$\frac{1}{T} = \left[\frac{\partial \phi}{\partial t}\right] = \left[-V_m k a (1 - K C_{aq})\right] = \frac{L^3}{M}\frac{M}{L^2 T}\frac{1}{L} = \frac{1}{T} \ . \tag{5.23}$$

In its discrete form, Eq. (5.22) can be written as:

$$\phi(t + \Delta t) = \phi(t) - V_m a k (1 - K C_{aq}) \Delta t \ . \tag{5.24}$$

In lattice units, the dimensionless volume of the rock node is discretely updated by:

$$\phi(t + \Delta t) = \phi(t) - V_m \tilde{k} (1 - K C_{aq}) \ , \tag{5.25}$$

where $\tilde{k} = k C_t / C_H = k a \Delta t$. For a more thorough analysis the reader is referred to Lichtner and Kang (2007), Appendix A.

6. MODEL VALIDATION

6.1 Diffusion and Reaction in a Rectangular Domain with Linear Reaction Kinetics

A diffusion-reaction simulation is carried out in a rectangular domain of size $a \times b$ (Kang and Lichtner, 2007). The reaction:

$$\mathrm{A} \rightleftharpoons \mathrm{A_{(s)}}$$

between the solute species, A, and solid species, $A_{(s)}$, occurs at the upper boundary ($y = b$) with first-order linear kinetics. Zero flux is imposed at the right ($x = a$) and lower boundary ($y = 0$). At the left boundary ($x = 0$), solute is allowed to diffuse into the domain, with a constant concentration. The steady-state solution to the diffusion reaction problem can be obtained using Laplace's equation:

$$\frac{\partial^2 C}{\partial x^2} + \frac{\partial^2 C}{\partial y^2} = 0 \,, \tag{6.1}$$

subject to the following boundary conditions:

$$r_D\Big|_{y=b} = -\mathcal{D}\frac{\partial C}{\partial y}\Big|_{y=b} = k_r\left(C|_{y=b} - C_{eq}\right) \,, \tag{6.2}$$

$$\frac{\partial C}{\partial y}\Big|_{y=b} = 0 \,, \tag{6.3}$$

$$C(0,y) = C_0 \,, \tag{6.4}$$

and

$$\left.\frac{\partial C}{\partial x}\right|_{x=a} = 0 \ . \tag{6.5}$$

An analytic solution for $C(x,y)$, under the above conditions has been obtained (Carslaw and Jaeger, 1986):

$$C(x,y) = (C_0 - C_{eq}) \sum_{n=0}^{\infty} \frac{\sin(\beta_n b)}{N_n^2 \beta_n} \frac{\cosh[\beta_n (x-a)]}{\cosh(\beta_n a)} \cos(\beta_n y) + C_{eq} \ , \tag{6.6}$$

where

$$N_n^2 = \frac{b}{2}\left(1 + \frac{\sin(2\beta_n b)}{2\beta_n b}\right) \ , \tag{6.7}$$

and β_n are obtained from the solutions of:

$$(\beta_n b)\tan(\beta_n b) = \frac{k_r b}{\mathcal{D}} \equiv Da \ . \tag{6.8}$$

The Damköhler number, Da, indicates the relative strength of reaction to diffusion. This choice of Damköhler number is described in more detail in Appendix C. The domain size chosen is 100×80. Initially, the domain is filled with solute in equilibrium with the solid with concentration C_{eq}, no reaction takes place. At time zero, the concentration at the boundary $x = 0$ is set to $C_0 > C_{eq}$. Diffusion and reaction begin to occur within the domain. The analytical solution along with the simulated solution is shown in **Fig. (6.1).** The other model parameters are given in **Table 6.1.**

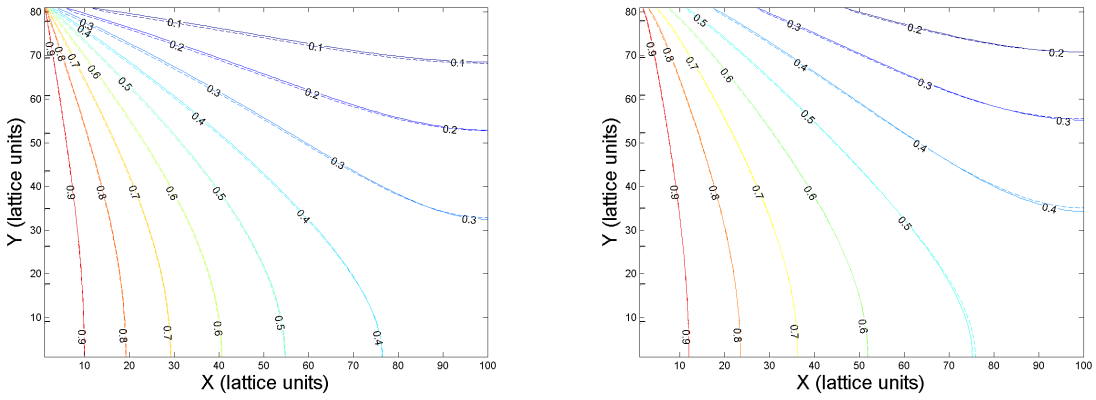

(a) (b)

Figure 6.1: Contours of equal solute concentration, at steady state, for (a) $Da = 48$ and (b) $Da = 4.8$ using the D2Q4 lattice. The solid and dashed lines denote the analytical solution and D2Q4 lattice results, respectively. The cavity size is 100×80 lattice units. At $x = 0$, the solute concentration C_0 is constant. Zero flux is imposed at the right ($x = a$) and lower boundaries ($y = 0$). The first-order linear reaction occurs at the upper boundary $y = b$.

Table 6.1: Parameters for $Da = 48$ and $Da = 4.8$.

	Lattice units
$\mathcal{D}$	$1/6$
τ	0.8333
$\mathbf{t_{max}}$	1×10^5
Da = 48	
k	0.1
C_0	10
C_{eq}	1
Da = 4.8	
k	0.01
C_0	10
C_{eq}	1

6.2 Diffusion and Reaction in a Closed Box

Exact mass transfer conversation is demonstrated by simulating diffusion and reaction in a closed box (Kang and Lichtner, 2007). **Fig. (6.2a)** shows the simulation domain with a dimension of 64×64 lattice units squared (LUS), corresponding to a physical domain size of 0.75×0.75 square centimeters. Two layers of solids are placed on each side of the domain. Initially, the pore space is partially filled with a solution containing species A. The concentration of A is set to zero for the 900 (30×30) pore nodes at the box's center. The remaining nodes are set in equilibrium with the box wall at a concentration of 0.1 mol/L. At each of the 240 solid/fluid interface nodes, the initial volume fraction of $A_{(s)}$ is set equal to 1 and reaction takes place according to Eq. (3.30).

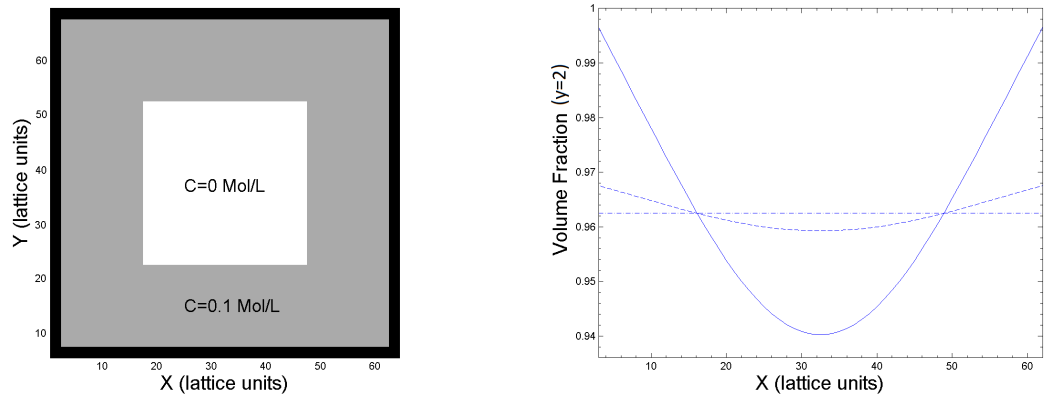

(a) (b)

Figure 6.2: (a) Simulation domain schematic for diffusion and reaction in a closed box. (b) Equilibrium distribution of the volume fraction of the boundary solid at the lower boundary ($y = 2$) for different Da numbers. The solid, dashed, and dashed-dotted lines denote the results for the D2Q4 lattice for $Da = 7.5 \times 10^{1}$, $Da = 7.5 \times 10^{-2}$, and $Da = 7.5 \times 10^{-5}$, respectively.

The molar volume is set to 0.1 L/mol. At equilibrium, the summation of the volume fraction of the interface nodes should be less than 240 because dissolution will have taken place. The difference in volume fraction should be exactly $900 \times 0.1 \times 0.1 = 9$ (i.e., the mass of solid dissolved is equal to that of the solute occupied by the 900 pore nodes). The dissolution distribution at the bottom of the box ($y = 2$), at equilibrium, is shown in **Fig. (6.2b)**. The relaxation time, τ, is set to 1. For the highest Damköhler number, the reaction is mass-transfer limited, and the dissolution rate is highest where the solution is renewed fastest by diffusion. As the *Da* decreases the reaction becomes surface-reaction limited. It is clear that for the lowest *Da* number, uniform dissolution occurs, leading to a straight horizontal line for the volume fraction distribution. Here, the value of the volume fraction is 0.9625, or 1-9/240, as should be expected.

6.3 Advection, Diffusion and Reaction in an Open Channel

This simulation is a comparison of the LB method with a FD method for flow in an open channel with reaction occurring at both channel walls (Kang and Lichtner, 2007). To validate the LB model, the thermal-hydrologic-chemical FD model, FLOTRAN, developed by Lichtner (1999), is used.

A prescribed Poisseuille (parabolic) profile is used, and the Péclet number ($uL/\mathcal{D}$) $Pe = 0.05 \times 60/0.1667 = 12$, where L is the characteristic height of the domain. The simulation size is 400×64 LUS, corresponding to a physical domain size of 5 cm in length and 0.75 cm in channel width. Two solid layers are placed at the top and bottom channel walls. Initially, the channel is filled with a solution containing species A and is in equilibrium with the channel wall consisting of $A_{(s)}$. A solution of negligible concentration (1×10^{-8} mol/L) is then injected from the right hand side and reaction takes place according to Eq. (3.30). The outlet is subject to a zero concentration gradient boundary condition. **Fig. (6.3)** shows the concentration distribution for $Da = 75$.

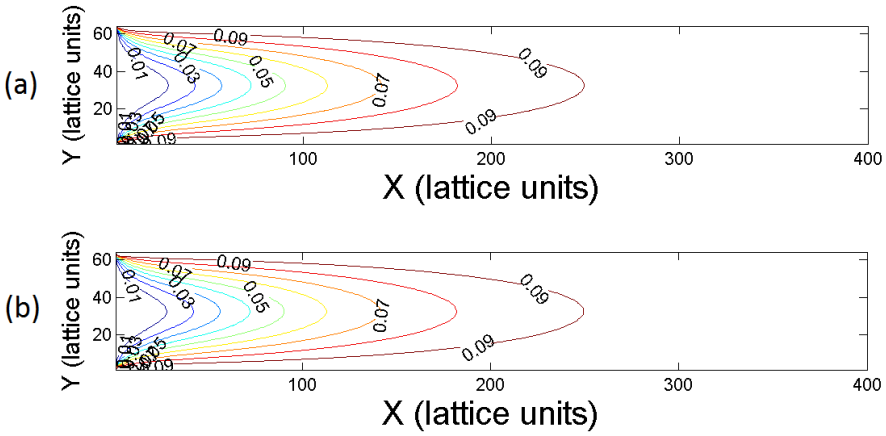

Figure 6.3: Concentration contours of (a) LB simulation and (b) FLOTRAN simulation results at $t = 1.95 \times 10^4$ s and with $Da = 75$. The root-mean-square deviation of the solute concentration is 5.4×10^{-4}, i.e., the agreement between the FLOTRAN and LB results is excellent. The equilibrium constant is $log(K_1) = 1$.

7. THERMAL FRACTURE ACIDIZING MODEL

7.1 Velocity Boundary Conditions

At the left inlet boundary, a uniform velocity is specified; a constant density (pressure) condition is specified at the right, top and bottom outlet boundaries (Zou and He, 1997). The flow rate at the inlet is 0.489 cm^3/s, assuming a 3D system of dimension $0.1 \times 0.1 \times 0.1$ cm^3.

7.2 Concentration Boundary Conditions

At the left inlet boundary, a constant concentration is specified; a zero concentration gradient is specified at the right, top, and bottom boundaries. The inlet concentration is 15% w/w HCl. The equilibrium concentration is 1×10^{-10} mol/L. The order of acid reaction at the boundary is given in **Table 4.1**. However, following the work of Kang et al. (2006); Kang and Lichtner (2007), the reaction kinetics remain linear here, i.e., $\alpha = 1$.

7.3 Temperature Boundary Conditions

In the following, simulations are carried out with constant (reservoir) temperature boundary conditions, specified at the top and bottom boundaries. Adiabatic conditions are specified at the right boundary (both formation and fracture). At the left boundary, adiabatic conditions are specified in the formation and constant (bottomhole) temperature in the fracture, i.e. assuming that cooler fluid is being injected. The rock and disconnected pore-space temperature are initialized to the reservoir temperature. The heat generated from the heterogeneous reaction is released into fluid nodes normal to the rock surface. In this study, only the reaction rate is temperature dependent. The other simulation paramaters (e.g., diffusion coefficient, thermal diffusivity, specific heat capacity) are kept constant; the variability of these parameters, with temperature, will be introduced in future in

work.

7.4 Reaction Rate Variation: 15% w/w HCl and Calcite

The fracture geometry can be imported as an image file and converted into a matrix of ones and zeros. In order to isolate the connected pore space the Matlab algorithm *bwconncomp* was used. This algorithm returns the connected components in a binary image. The component connecting the inlet to the outlet can then be isolated and used to calculate the effective porosity of the fracture and model the temperature-dependent acid reaction.

Simulations are carried out with the above boundary conditions. The temperature of the injected fluid and reservoir are 300 ^{o}K and 339 ^{o}K, respectively. Steady-state flow is achieved prior to acid injection. As acid is injected, the fracture surface dissolves and the fracture geometry is continuously updated, resulting in local unsteady-state flow. The heat released from the reaction causes an increase in fluid temperature at the fracture surface (and is convected into the pore space). This results in an increase in the reaction rate constant, by Eq. (4.20), thus increasing the dissolution rate (Eq. (5.22)).

The reaction rate and diffusion coefficient for a 15% w/w HCl-calcite reaction are $k_{r,T_0} = 0.1$ cm/s and $\mathcal{D} = 1 \times 10^{-4}$cm^2/s, respectively, at $T_0 = 288.56$ ^{o}K (Settari, 1993). The heat of reaction is 9.5 kcal/g mole $CaCO_3$ and the thermal conductivity of the fluid and rock are $\kappa_f = 1.24 \times 10^{-3}$ cal/s cm ^{o}C and $\kappa_r = 5.78 \times 10^{-3}$ cal/s cm ^{o}C, respectively (Lee and Roberts, 1980).

7.4.1 Simple Geometry

The initial formation geometry, as shown in **Fig. (7.1a)**, is entirely solid. The lattice spacing is 5.4×10^{-6}m. The lattice dimensions are, $l_x \times l_y = 186 \times 186$ representing a 0.1×0.1 cm^2 domain. **Fig. (7.1b)** shows the formation with an induced fracture of width 0.03 cm. The Reynolds number for flow between two parallel plates is given by (Rothfus

et al., 1957):

$$Re = \frac{u(2L)}{\nu} = \frac{2 \times 10^{-2}(2)(3 \times 10^{-4})}{1 \times 10^{-6}} = 12 \tag{7.1}$$

where L is the characteristic heigth between the plates, u is the average velocity, and ν is the kinematic viscosity. For flow between two parallel plates, a Reynolds number below 1800 results in laminar flow (Lee and Roberts, 1980). The LB method is also capable of modeling turbulent flow.

During each of the following simulations, the flow rate will remain constant and thus the Péclet number will also. For example, the local fracture height may increase but the local velocity will then decrease.

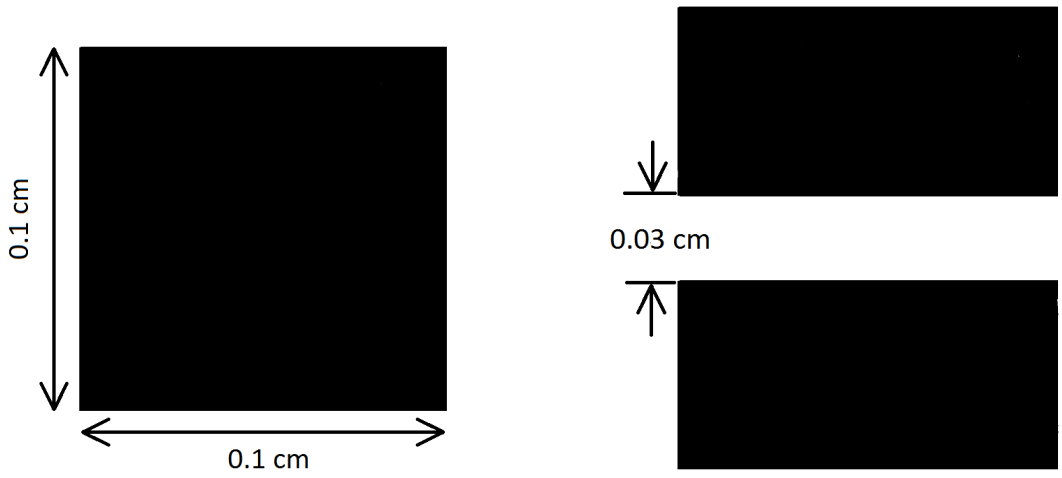

(a) (b)

Figure 7.1: (a) The initial formation geometry. (b) The formation geometry after the fracture has been induced. The white region represents the total fracture space (the inlet and outlet are to the left and right, respectively) and black represents the rock.

Fig. (7.2) illustrates the fluid-filled fracture sample.

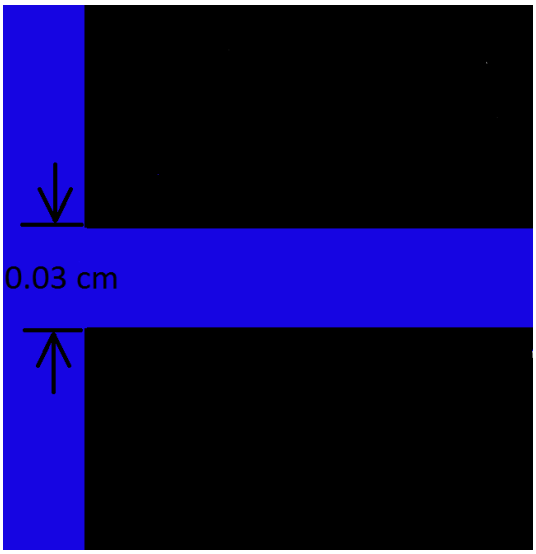

Figure 7.2: The initial formation geometry. The blue region represents the injected fluid, black represents the rock.

The concentration distribution and fracture dissolution with time are illustrated in **Fig. (7.3)**. **Figs. (7.4a) and (7.4b)** compare the concentration distribution without and with the temperature effects, respectively. In Fig. (7.4b), the reaction rate is increased and, as a result, the acid is consumed at a higher rate as it flows through the pore space. **Fig. (7.4c)** shows the velocity distribution without the effect of temperature while **Fig. (7.4d)** shows the same but with the effect of temperature. The temperature distribution and an overlap of the fracture geometries, to highlight the additional dissolution, are shown in **Figs. (7.5a) and (7.5b)**, respectively.

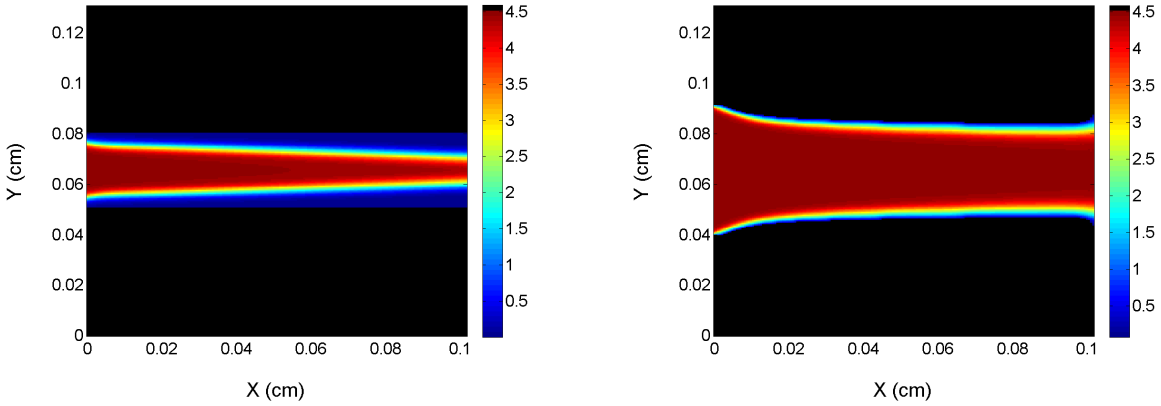

(a)

(b)

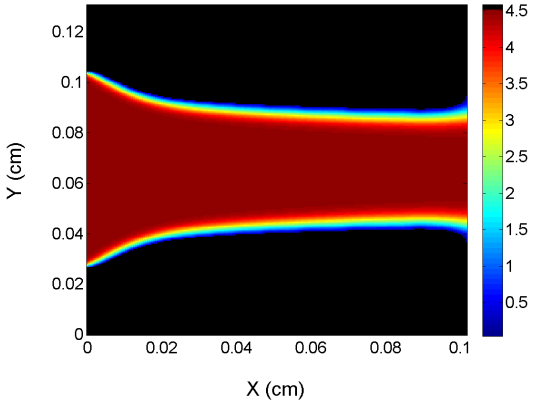

(c)

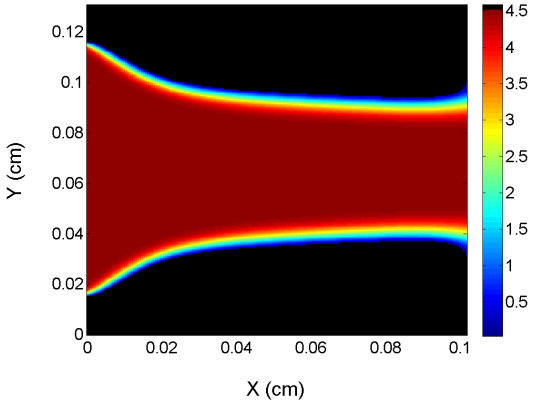

(d)

Figure 7.3: Dissolution of fracture geometry with time (a $\rightarrow$ b $\rightarrow$ c $\rightarrow$ d), with temperature effects included. The colorbar represents the acid concentration in units of mol/L.

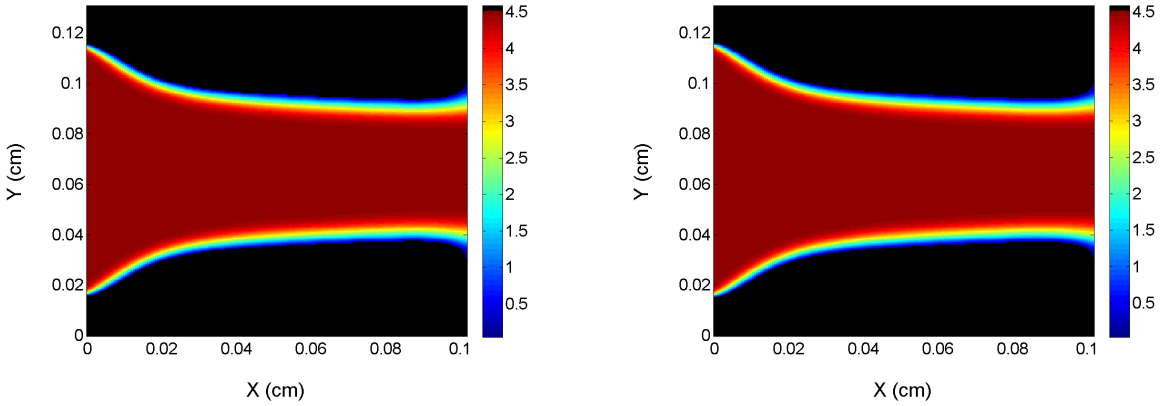

(a)

(b)

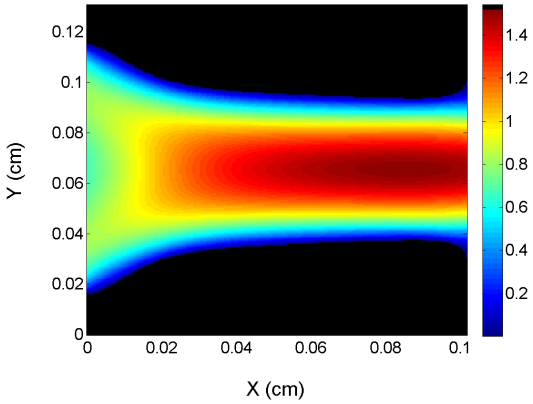

(c)

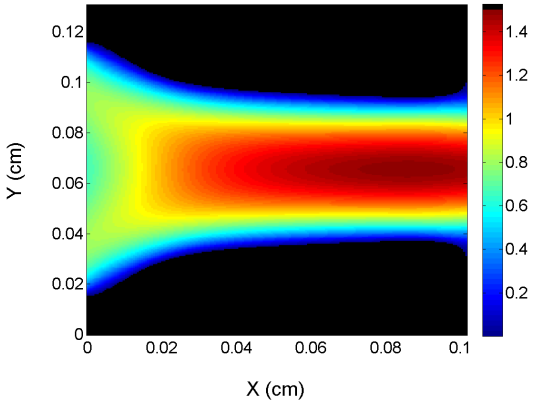

(d)

Figure 7.4: Top: Final acid concentration distribution, (a) without temperature effects and (b) with temperature effects. The colorbar is in units of mol/L. Bottom: Velocity distribution for varying reaction rate, (c) without temperature effects and, (d) with temperature effects. The colorbar is in units of cm/s.

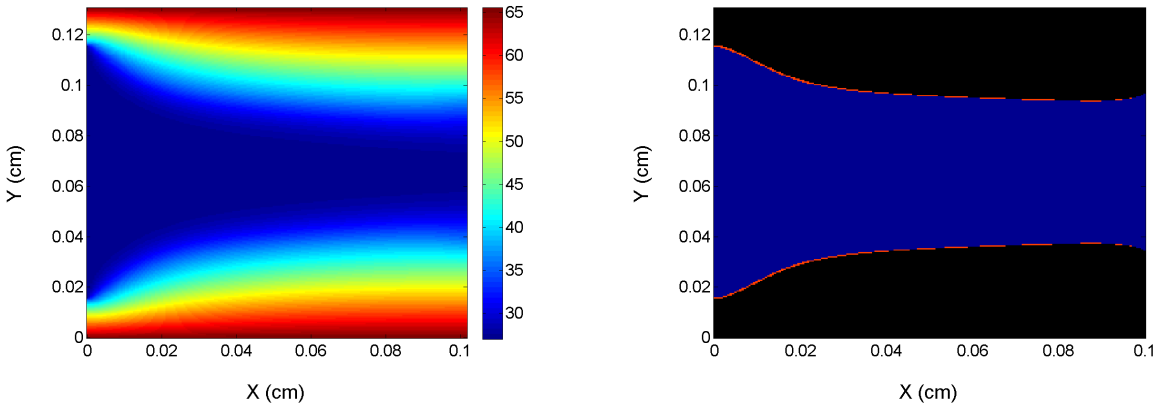

(a) (b)

Figure 7.5: (a) Final temperature distribution in the fracture. The colorbar is in units of degrees Celsius. (b) An overlap of the fracture geometries, with and without the effect of temperature. The red outline highlights the additional dissolution caused by the reaction rate increase.

7.4.2 Complex Geometry

The initial formation geometry, as shown in **Fig. (7.6a)**, is composed of solid and fluid nodes with a porosity of 28%. The lattice spacing is 5.4×10^{-6}m. The lattice dimensions are, $l_x \times l_y = 186 \times 186$ representing a 0.1×0.1 cm^2 domain. **Fig. (7.6b)** shows the formation with an induced fracture of width 0.03 cm.

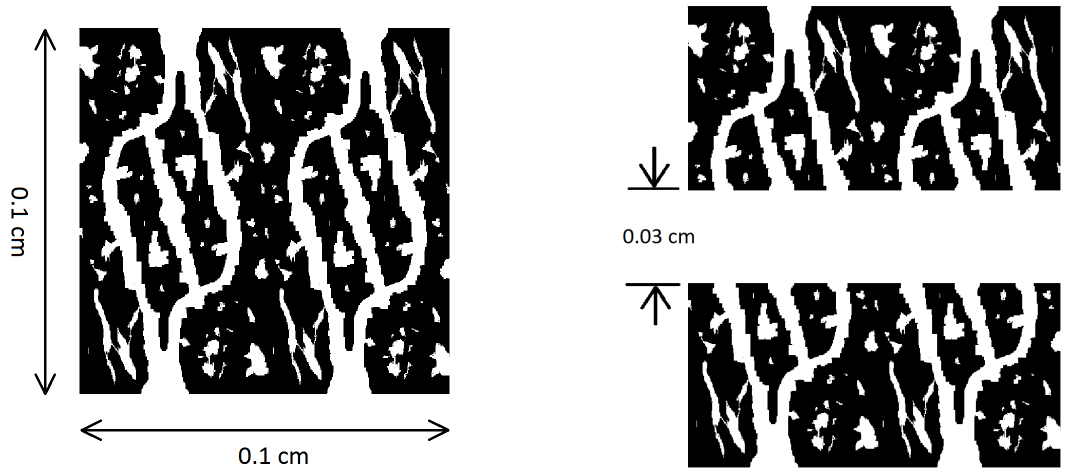

(a) (b)

Figure 7.6: (a) The initial formation geometry. (b) The formation geometry after the fracture has been induced. The white region represents the total fracture and pore space (the inlet and outlet are to the left and right, respectively) and black represents the rock.

The Matlab algorithm *bwconncomp* is used to return the connected components in a binary image. The component connecting the inlet to the outlet can then be isolated and used to calculate the effective porosity of the fracture and model the temperature-dependent acid reaction. **Fig. (7.7)** illustrates the fluid-filled (connected) pore space of the fracture sample.

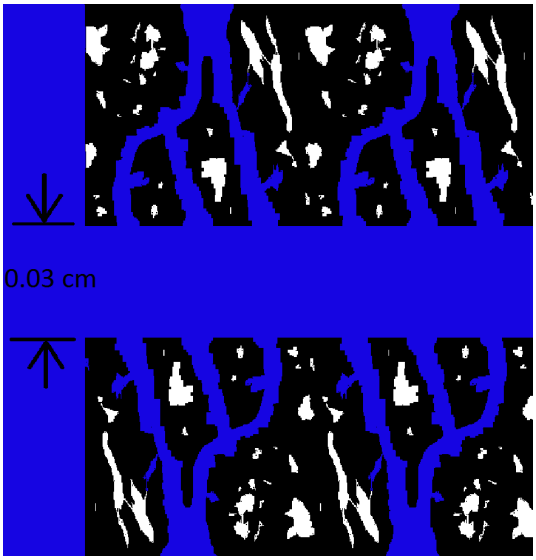

Figure 7.7: The initial formation geometry. The blue region represents the injected fluid, black represents the rock, and the white represents disconnected pore space.

The concentration distribution and fracture dissolution with time are illustrated in **Fig. (7.8)**. **Figs. (7.9a) and (7.9b)** compare the concentration distribution without and with the temperature effects, respectively. In Fig. (7.9b), the reaction rate is increased and, as a result, the acid is consumed at a higher rate as it flows through the pore space. **Fig. (7.9c)** shows the velocity distribution without the effect of temperature while **Fig. (7.9d)** shows the same but with the effect of temperature. The temperature distribution and an overlap of the fracture geometries, to highlight the additional dissolution, are shown in **Figs. (7.10a) and (7.10b)**, respectively.

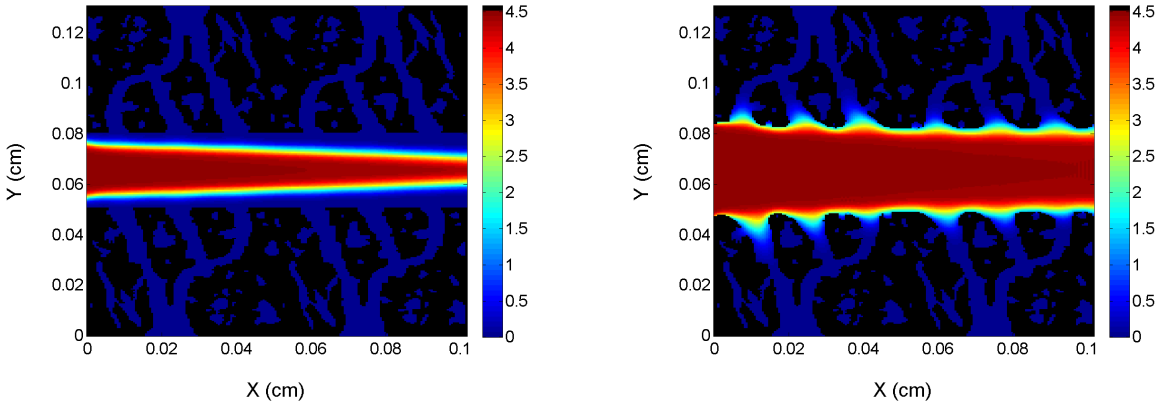

(a) (b)

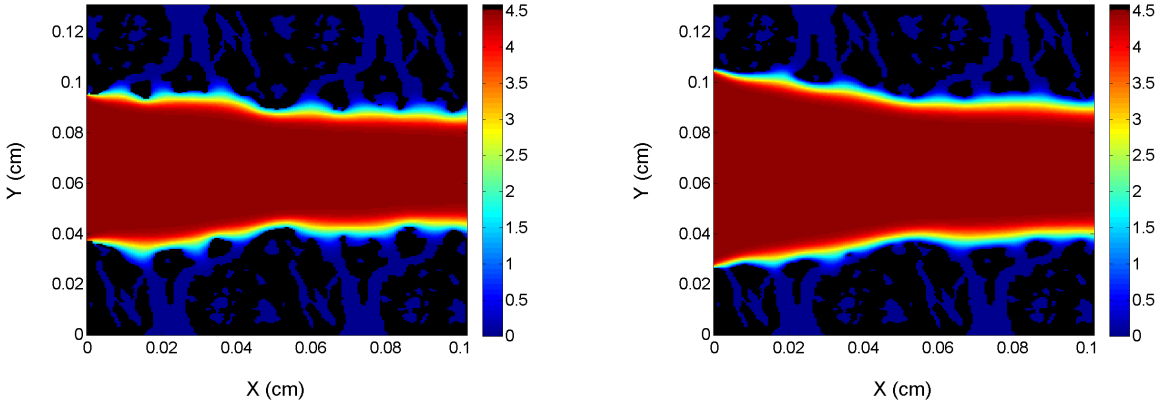

(c) (d)

Figure 7.8: Dissolution of fracture geometry with time (a $\rightarrow$ b $\rightarrow$ c $\rightarrow$ d), with temperature effects included. The colorbar represents the acid concentration in units of mol/L.

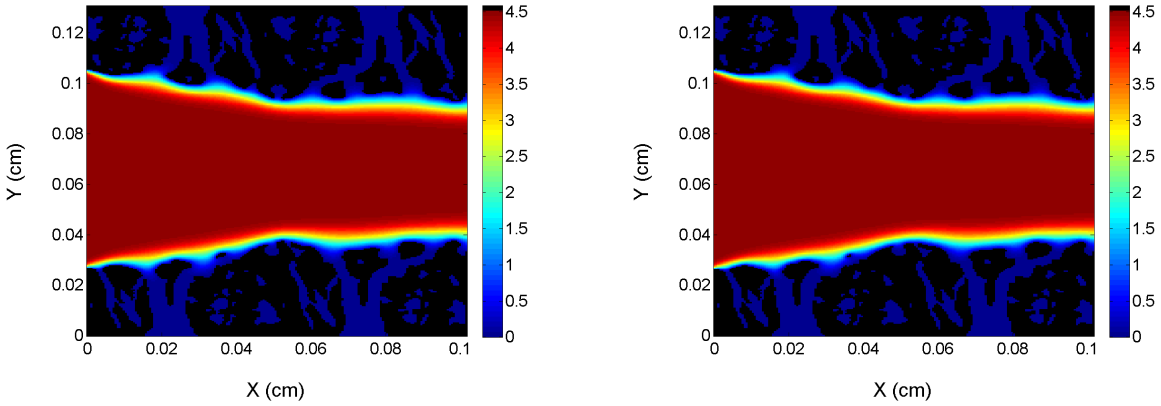

(a) (b)

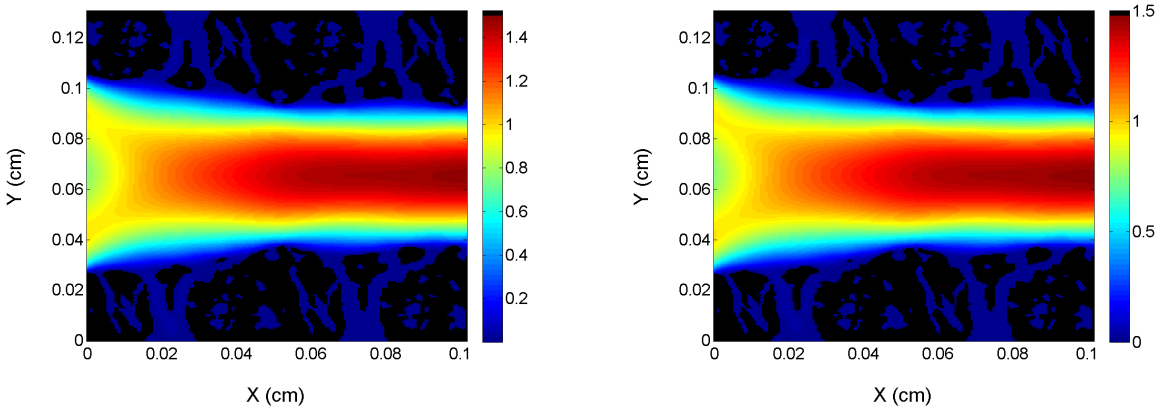

(c) (d)

Figure 7.9: Top: Final acid concentration distribution, (a) without temperature effects and (b) with temperature effects. The colorbar is in units of mol/L. Bottom: Velocity distribution for varying reaction rate, (c) without temperature effects and, (d) with temperature effects. The colorbar is in units of cm/s.

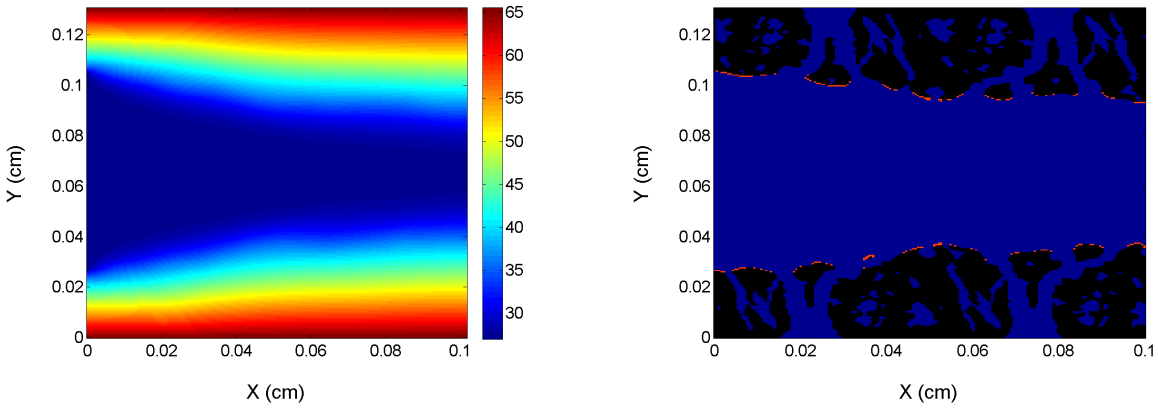

(a) (b)

Figure 7.10: (a) Final temperature distribution in the fracture. The colorbar is in units of degrees Celsius. (b) An overlap of the fracture geometries, with and without the effect of temperature. The red outline highlights the additional dissolution caused by the reaction rate increase.

Following acidizing, the two the two fractures, with and without temperature effects, are then closed again. The resulting geometries are shown in **Fig. (7.11)**.

(a) (b)

Figure 7.11: (a) Final fracture geometry without temperature effects included. (b) Final fracture geometry with temperature effects included.

7.5 Reaction Rate Variation: 28% w/w HCl and Calcite

The reaction rate for a 28% w/w HCl-calcite reaction is $k_{r,T_0} = 4.129 \times 10^{-4}$ cm/s, at $T_0 = 310.77$ ^{o}K (Settari, 1993). Due to a lack of data, the diffusion coefficient is assumed to be equal to that of the 15% HCl solution, $\mathcal{D} = 1 \times 10^{-4} \text{cm}^2/\text{s}$. The heat of reaction is 9.5 kcal/g mole $CaCO_3$ and the thermal conductivity of the fluid and rock are $\kappa_f = 1.24 \times 10^{-3}$ cal/s cm ^{o}C and $\kappa_r = 5.78 \times 10^{-3}$ cal/s cm ^{o}C, respectively (Lee and Roberts, 1980). The complex geometry is used in this simulation.

The concentration distribution and fracture dissolution with time are illustrated in **Fig. (7.12)**. **Figs. (7.13a) and (7.13b)** compare the concentration distribution without and with the temperature effects, respectively. In Fig. (7.13b), the reaction rate is increased and, as a result, the acid is consumed at a higher rate as it flows through the pore space. **Fig. (7.13c)** shows the velocity distribution without the effect of temperature while **Fig. (7.13d)** shows the same but with the effect of temperature. The temperature distribution and an overlap of the fracture geometries, to highlight the additional dissolution, are shown in **Figs. (7.14a) and (7.14b)**, respectively.

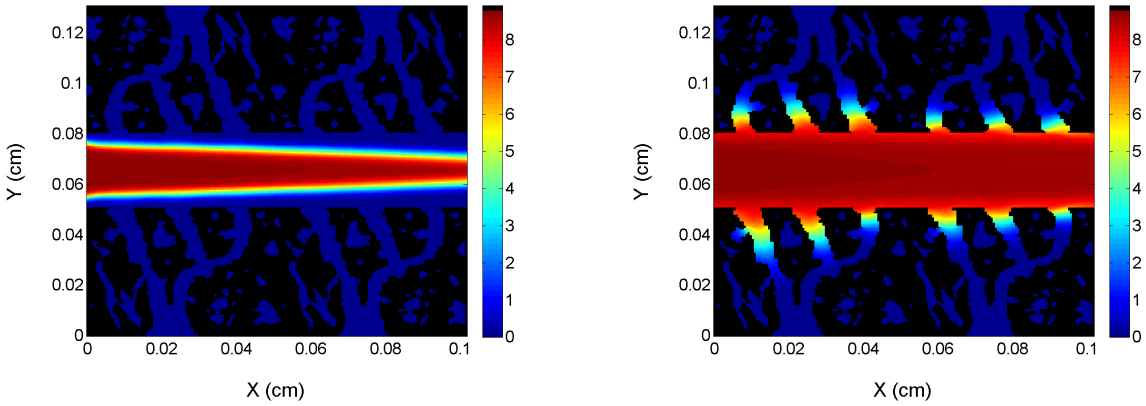

(a) (b)

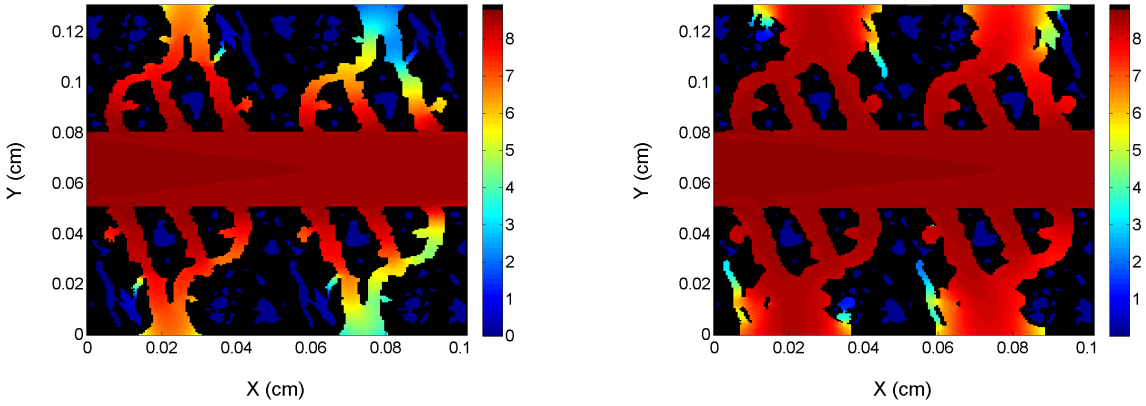

(c) (d)

Figure 7.12: Dissolution of fracture geometry with time (a $\rightarrow$ b $\rightarrow$ c $\rightarrow$ d), with temperature effects included. The colorbar represents the acid concentration in units of mol/L.

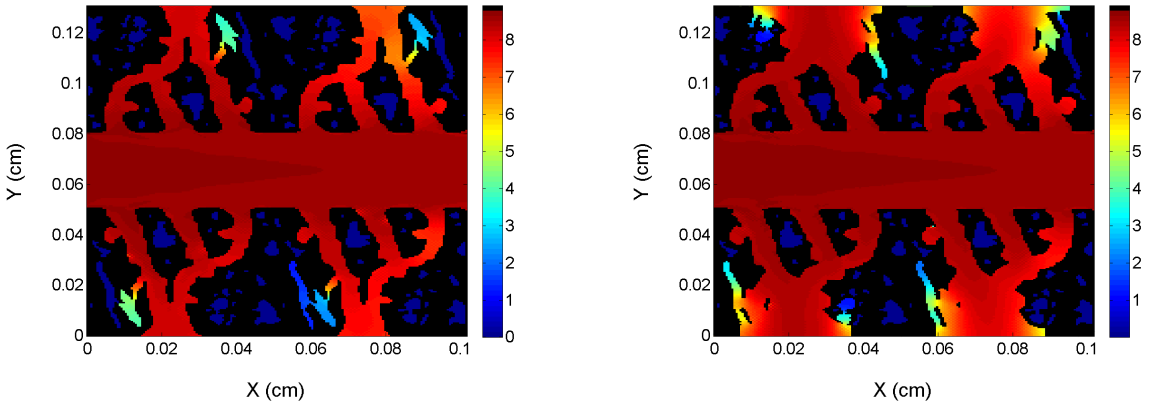

(a)

(b)

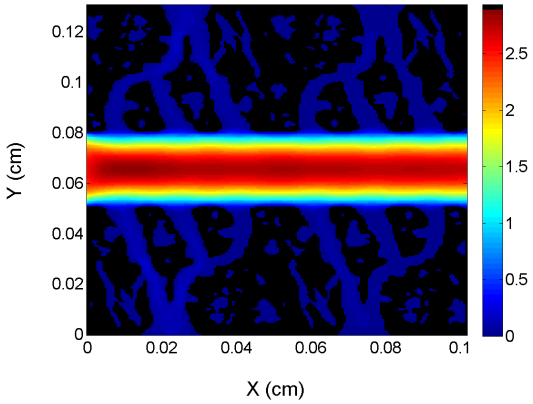

(c)

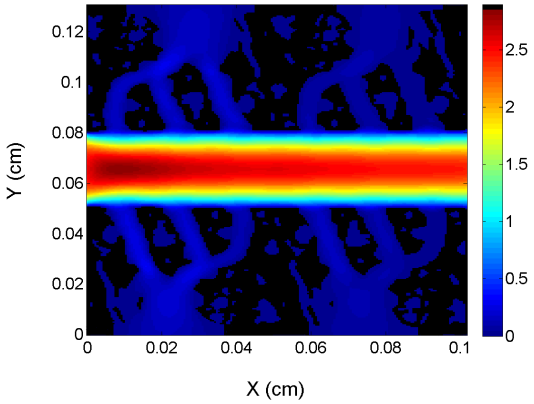

(d)

Figure 7.13: Top: Final acid concentration distribution, (a) without temperature effects and (b) with temperature effects. The colorbar is in units of mol/L. Bottom: Velocity distribution for varying reaction rate, (c) without temperature effects and, (d) with temperature effects. The colorbar is in units of cm/s.

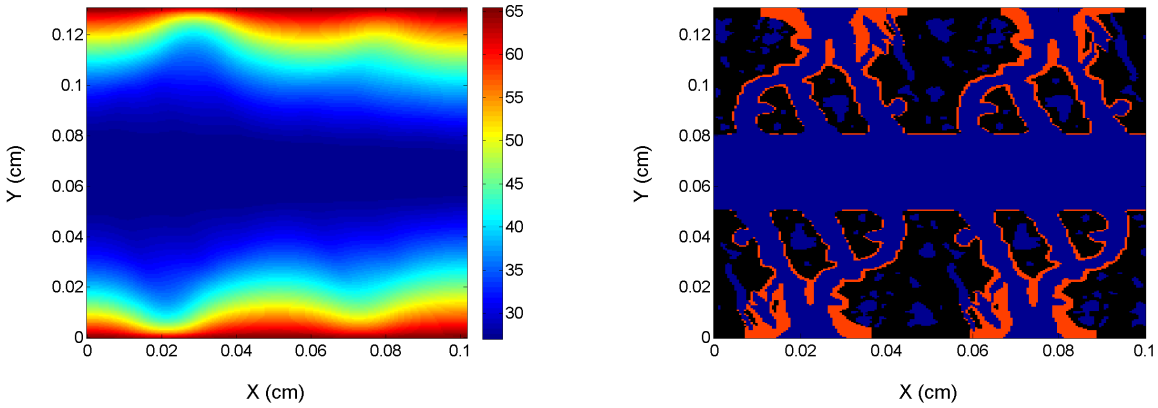

(a) (b)

Figure 7.14: (a) Final temperature distribution. The black color represents the fracture matrix, and the blue represents pore space. The colorbar is in units of degrees Celsius. (b) An overlap of the fracture geometries, with and without the effect of temperature. The red outline highlights the additional dissolution caused by the reaction rate increase.

8. CONCLUSIONS AND RECOMMENDATIONS

During the development of this research, the following conclusions were reached:

1. The lattice-Boltzmann finite-difference model has proven to be successful at describing thermal reactive transport in arbitrary fracture geometries, on a pore-scale level
2. The model has been validated against an analytical solution and a previous advection-reaction finite difference study. It has also been shown to exhibit exact mass-transfer in a closed system
3. It has been shown that increased reaction rates, due to temperature effects, result in greater fracture dissolution and likely increased fracture conductivity. In diffusion-limited acid-rock systems, increasing the surface reaction rate (resulting from an increase in temperature) does not result in an increase in dissolution rate. However, when the system is surface reaction rate limited, increasing the temperature does increase the dissolution rate
4. Arbitrary geometries can be easily implemented using greyscale or black/white images
5. A wide range of values for the fracture acidizing parameters (e.g., Péclet number, Damköhler number, downhole and reservoir temperatures) can be modeled
6. The finite-difference temperature-distribution update can be carried out using the same lattice spacing and lattice time step as used in the velocity- and concentration-distribution updates
7. In order to accurately predict fracture conductivity following acid injection, temperature effects should be taken into account

The proposed recommendations and future work related to this project are:

1. Add rock mineralogy heterogeneity, i.e., regions with higher and lower reaction rates, calculate the fracture conductivity, and validate or modify existing conductivity correlations. A comparison of conductivity with and without temperature effects can also be carried out
2. Introduce non-linear reaction kinetics
3. Scale the simulation up to model an entire fractured formation. Work on scaling up the LB method is underway (Lichtner and Kang, 2007; Chen et al., 2013)
4. Extend the present model to three dimensions
5. Extend the present model to also investigate the effect of temperature on the acid diffusion coefficient, thermal diffusivity, and specific heat capacity
6. Run the simulation in parallel: the lattice Boltzmann method is highly parallelizable
7. Further analysis into the effect of no-slip velocities for low Knudsen numbers and adding a slip velocity, where required
8. Import CT scans of fractured rock and model a physical example. An input binary matrix can be obtained using laboratory CT scans (e.g., **Fig. (8.1)**) and imaging software with data filtering and segmentation techniques. A matrix (lattice) can then be constructed such that each value of 1 would correspond to a fluid node and the remaining values (zeros) would be solid nodes

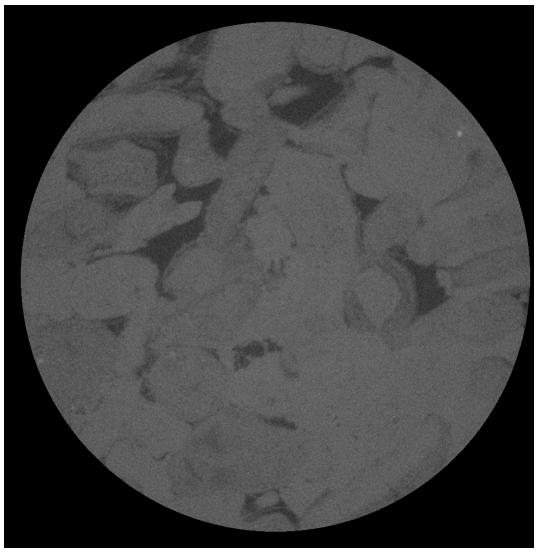

Figure 8.1: A CT scan of a carbonate rock core. The dark areas represent pore space.

BIBLIOGRAPHY

B. Alazmi and V. Kambiz. Constant wall heat flux boundary conditions in porous media under local thermal non-equilibrium conditions. *International Journal of Heat and Mass Transfer*, 45:30713087, 2002.

L. F. Antelo, M. Pournik, Zhu D., and A. D. Hill. Surface etching pattern and its effect on fracture conductivity in acid fracturing. *SPE*, 119743, 2009.

C. S. N. Azwadi and T. Tanahashi. Simplified finite difference thermal lattice boltzmann method. *International Journal of Modern Physics B*, 22:3865–3876, 2008.

A. N. Barron, A. R. Hendrickson, and D. R. Wieland. The effect of flow on acid reactivity in a carbonate fracture. *Journal of Petroleum Technology*, SPE 134:409, 1962.

R. Benzii and S. Succi. The lattice boltzmann equation: Theory and applications. *Physics Reports (Review Section of Physics Letters)*, 222:145–197, 1992.

M. Buijse, P. de Boer, B. Breukel, and G. Burgos. Organic acids in carbonate acidizing. *SPE*, 82211, 2004.

H. S. Carslaw and J.C. Jaeger. *Conduction of Heat in Solids*. Oxford Univ. Press, New York., 1986.

H. Chen, S. Chen, and W. H. Matthaeus. Recovery of the navier-stokes equations using a lattice-gas boltzmann method. *Phys. Rev. A.*, 45:R533942, 1992.

L. Chen, Q. Kang, B. A. Robinson, Y. A. He, and W. Q. Tao. Pore-scale modeling of multiphase reactive transport with phase transitions and dissolution-precipitation processes in closed systems. *Phys. Rev. E*, 87:043306, 2013.

S. P. Dawson, S. Chen, and G. D. Doolen. Lattice boltzmann computations for reaction-diffusion equations. *J. Chem. Phys.*, 98:1514, 1993.

W. B. Durham, W. L. Bourcier, and E. A. Burton. Direct observation of reactive flow in a single fracture. *Water Resources Research*, 37(1):1–12, 2001.

M. J. Economides and K. G. Nolte. *Reservoir Stimulation, 3rd Edition*. Wiley & Sons Ltd., West Sussex, England, 2000.

C. N. Fredd and H. S. Fogler. Influence of transport and reaction on wormhole formation in porous media. *Fluid Mechanics and Transport Phenomena*, 44, 9:1933–1949, 1998.

U. Frisch, B. Hasslacher, and Y. Pomeau. Lattice-gas automata for the navier-stokes equation. *Physical Review Letters*, 56, no. 14:1505–1506, 1986.

M. Gong, S. Lacote, and A. D. Hill. A new model of acid fracture conductivity based on deformation of surface asperities. *SPE 39431*, pages 133–147, 1998.

J. Hardy, Y. Pomeau, and O. de Pazzis. Time evolution of a two-dimensional classical lattice system. *Physical Review Letters*, 31:276–279, 1973.

X. He, N. Li, and B. Goldstein. Lattice boltzmann simulation of diffusion-convection systems with surface chemical reaction. *Molecular Simulation*, 25:3-4:145–156, 2000.

F. J. Higuera and J. Jiménez. Boltzmann approach to lattice gas simulations. *Europhys. Lett.*, 9:663, 1989.

F. J. Higuera, S. Succi, and R. Benzii. Lattice gas dynamics with enhanced collisions. *Europhys. Lett.*, 9:345, 1989.

M. Jami, A. Mezrhab, M. Bouzidib, and P. Lallemand. Lattice-boltzmann computation of natural convection in a partitioned enclosure with inclined partitions attached to its hot wall. *Physica A*, 368:481494, 2006.

M. Junk. A finite difference interpretation of the lattice boltzmann method. *Inc. Numer Methods Partial Differential Eq*, 17:383–402, 2001.

M. Junk and A. Klar. Discretizations for the incompressible navier-stokes equations based on the lattice boltzmann method. *SIAM J. SCI. COMPUT.*, 22:1–19, 2000.

Q. Kang and P. C. Lichtner. An improved lattice boltzmann model for multicomponent reactive transport in porous media at the pore scale. *Water Resources Research*, 43: W12S14, 2007.

Q. Kang, D. Zhang, S. Chen, and X. He. Lattice boltzmann simulation of chemical dissolution in porous media. *Phys. Rev. E*, 65:036318, 2002.

Q. Kang, D. Zhang, and S. Chen. Simulation of dissolution and precipitation in porous media. *J. Geophys. Res.*, 108:B102505, 2003.

Q. Kang, P. C. Lichtner, and D. Zhang. Lattice boltzmann pore-scale model for multicomponent reactive transport in porous media. *Journal of Geophysical Research*, 111: B05203, 2006.

I. Kim, W. B. Lindquist, and W. B. Durham. Fracture flow simulation using a finite-difference lattice boltzmann method. *Physical Review E.*, 67:046708, 2003.

M. H. Kim, C. S. Kim, H. W. Lee, and K. Kim. Temperature dependence of dissociation constants for formic acid and 2,6=dinitrophenol in aqueous solutions up to 175 ”c. *J. Chem. SOC., Faraday Trans.*, 92(24):4951–4956, 1996.

P. Lallemand and L. Luo. Theory of the lattice boltzmann method: Acoustic and thermal properties in two and three dimensions. *Phys. Rev. E*, 68:036706, 2003a.

P. Lallemand and L. S. Luo. Hybrid finite-difference thermal lattice boltzmann equation. *International Journal of Modern Physics*, 17(1-2):41–47, 2003b.

M. H. Lee and L. D. Roberts. Effect of heat of reaction on temperature distribution and acid penetration in a fracture. *SPE*, pages 501–507, 1980.

L. Li, H. A. Nasr-El-Din, T. T. Chang, and T. Lindvig. Reaction of simple organic acids and chelating agents with calcite. *SPE*, IPTC 12886, 2008.

P. C. Lichtner. Flotran users guide, report. *Los Alamos Natl. Lab., Los Alamos, N. M.*, 1999.

P. C. Lichtner and Q. Kang. Upscaling pore-scale reactive transport equations using a multiscale continuum formulation. *Water Resources Research*, 43:W12S15, 2007.

K. K. Lo and R. H. Dean. Modeling of acid fracturing. *SPE Production Engineering*, 4(2): 194–200, 1989.

K. Lund, H. S. Fogler, and C. C. McCune. Acidization - i. the dissolution of dolomite in hydrochloric acid. *Chemical Engineering Science*, Vol. 28:pp. 691–700, 1973.

K. Lund, H. S. Fogler, C. C. McCune, and J. W. Ault. Acidization - ii. the dissolution of calcite in hydrochloric acid. *Chemical Engineering Science*, Vol. 30:pp. 825–335, 1975.

G. R. McNamara and G. Zanetti. Use of the boltzmann equation to simulate lattice-gas automata. *Phys. Rev. Lett.*, 61:23322335, 1988.

A. Mezrhab, M. Bouzidi, and P. Lallemand. Hybrid lattice-boltzmann finite-difference simulation of convective flows. *Computers & Fluids*, 33:623641, 2004.

A. Mezrhab, M. A. Moussaoui, and H. Naji. Lattice boltzmann simulation of surface radiation and natural convection in a square cavity with an inner cylinder. *J. Phys. D*, 41:115502, 2008.

M. A. Moussaoui, M. Jami, A. Mezrhab, and H. Naji. Convective heat transfer over two blocks arbitrary located in a 2d plane channel using a hybrid lattice boltzmann-finite difference method. *Heat Mass Transfer*, 45:13731381, 2009.

D. E. Nierode and K. F. Kruk. An evaluation of acid fluid loss additives, retarded acids, and acidized fracture conductivity. *SPE 4549*, 1973.

D. E. Nierode and B. B. Williams. Characteristics of acid reaction in limestone formations. *SPE*, SPE 3101, 1971.

D. R. Noble. Lattice boltzmann study of the interstitial hydrodynamics and dispersion in steady inertial flows in large randomly packed beds. *Ph.D. thesis, Univ. of Ill. at Urbana-Champaign, Urbana.*, 1997.

M. Pournik, C. Zou, C. Malagon Nieto, M. G. Melendez, D. Zhu, and A. D. Hill. Small-scale fracture conductivity created by modern acid-fracture fluids. *SPE 106272*, 2007.

R. R. Rothfus, D. H. Archer, I. C. Kumas, and K. G. Sikchi. Simplified flow calculations for tubes and parallel plates. *A.I.Ch.E.*, June:208, 1957.

C. S. Ruffet, J-J. Féry, and A. Onaisi. Acid-fracturing treatment: A surface-topography analysis of acid-etched fractures to determine residual conductivity. *SPE Journal*, pages 155–162, June, 1998.

R. S. Schechter. *Oil Well Stimulation*. Prentice Hall, New Jersey, 1992.

A. Settari. Modeling of acid-fracturing treatments. *SPE Production & Facilities*, 8(1): 30–38, 1993.

A. Settari, R. B. Sullivan, and C. Hansen. A new two-dimensional model for acid-fracturing design. *SPE Production & Facilities*, 16(4):200–209, 2001.

S. Succi. *The Lattice Boltzmann Equation for Fluid Dynamics and Beyond.* Clarendon Press, Oxford, England, 2001.

M. Sukop and D. Thorne. *Lattice Boltzmann Modeling.* Springer- Verlag Berlin Heidelberg, 2010.

P. Szymczak and A. C. Ladd. Wormhole formation in dissolving fractures. *J. Geophys. Res.*, 114:B06203, 2009.

P. Szymczak and A. C. Ladd. Instabilities in the dissolution of a porous matrix. *Geophysical Research Letters*, 38:L07403, 2011.

R. Verberg and A. C. Ladd. Simulation of low-reynolds-number flow via a time-independent lattice-boltzmann method. *Phys. Rev. E.*, 60(3):3367, 1999.

B. B. Williams and D. E. Nierode. Design of acid fracturing treatments. *JPT*, page 849, 1972.

Q. Zou and X He. On pressure and velocity boundary conditions for the lattice boltzmann bgk model. *Phys. Fluids*, 9:1591–1598, 1997.

APPENDIX A

BOUNDARY CONDITIONS FOR IMPLICIT TEMPERATURE UPDATE

The assumed flow direction is u_x in the i-direction and u_y in the j-direction, based on the definition of the finite-difference equations. The implicit formulation can be written as:

$$T_{i,j}^{k} = T_{i,j}^{k+1} + \left(\frac{\Delta t}{\Delta x}\right)(u_x \partial_x^* T + u_y \partial_y^* T)^{k+1} - \left(\kappa \frac{\Delta t}{\Delta x^2}\right)\Delta^* T^{k+1}. \tag{A.1}$$

Written out fully and factorized this becomes:

$$\begin{aligned} T_{i,j}^{k} &= (u_x q - 2r)T_{i+1,j}^{k+1} - (u_x q + 2r)T_{i-1,j}^{k+1} + (u_y q - 2r)T_{i,j+1}^{k+1} \\ &- (u_y q + 2r)T_{i,j-1}^{k+1} + (-0.25q[u_x + u_y] + 0.5r)T_{i+1,j+1}^{k+1} \\ &+ (0.25q[u_x - u_y] + 0.5r)T_{i-1,j+1}^{k+1} + (0.25q[u_x + u_y] + 0.5r)T_{i-1,j-1}^{k+1} \\ &+ (0.25q[-u_x + u_y] + 0.5r)T_{i+1,j-1}^{k+1} + (1 + 6r)T_{i,j}^{k+1} \ . \end{aligned} \tag{A.2}$$

A.1 Constant Temperature Boundaries

At the boundary where $i = 1$,

$$\begin{aligned} T_{1,j}^{k} &= (u_x q - 2r)T_{2,j}^{k+1} - (u_x q + 2r)T_{0,j}^{k+1} + (u_y q - 2r)T_{1,j+1}^{k+1} \\ &- (u_y q + 2r)T_{1,j-1}^{k+1} + (-0.25q[u_x + u_y] + 0.5r)T_{2,j+1}^{k+1} \\ &+ (0.25q[u_x - u_y] + 0.5r)T_{0,j+1}^{k+1} + (0.25q[u_x + u_y] + 0.5r)T_{0,j-1}^{k+1} \\ &+ (0.25q[-u_x + u_y] + 0.5r)T_{2,j-1}^{k+1} + (1 + 6r)T_{1,j}^{k+1} \ , \end{aligned} \tag{A.3}$$

and for $i = 0$, $T_{0,j} = T_{Ht}$,

$$\begin{aligned} T \quad & {}^{k}_{1,j} + (u_x q + 2r)T_{Ht} - (0.25q[u_x - u_y] + 0.5r)T_{Ht} \\ - \quad & (0.25q[u_x + u_y] + 0.5r)T_{Ht} \\ = \quad & (u_x q - 2r)T^{k+1}_{2,j} + (u_y q - 2r)T^{k+1}_{1,j+1} - (u_y q + 2r)T^{k+1}_{1,j-1} \\ + \quad & (-0.25q[u_x + u_y] + 0.5r)T^{k+1}_{2,j+1} + (0.25q[-u_x + u_y] + 0.5r)T^{k+1}_{2,j-1} \\ + \quad & (1 + 6r)T^{k+1}_{1,j} \ , \end{aligned} \tag{A.4}$$

and thus:

$$\begin{aligned} T^{k}_{1,j} + (0.5qu_x + r)T_{Ht} \quad = \quad & (u_x q - 2r)T^{k+1}_{2,j} + (u_y q - 2r)T^{k+1}_{1,j+1} \\ - \quad & (u_y q + 2r)T^{k+1}_{1,j-1} + (-0.25q[u_x + u_y] + 0.5r)T^{k+1}_{2,j+1} \\ + \quad & (0.25q[-u_x + u_y] + 0.5r)T^{k+1}_{2,j-1} + (1 + 6r)T^{k+1}_{1,j} \ . \end{aligned} \tag{A.5}$$

At the boundary where $i = N_i$,

$$\begin{aligned} T^{k}_{N_i,j} \quad = \quad & (u_x q - 2r)T^{k+1}_{N_i+1,j} - (u_x q + 2r)T^{k+1}_{N_i-1,j} + (u_y q - 2r)T^{k+1}_{N_i,j+1} \\ - \quad & (u_y q + 2r)T^{k+1}_{N_i,j-1} + (-0.25q[u_x + u_y] + 0.5r)T^{k+1}_{N_i+1,j+1} \\ + \quad & (0.25q[u_x - u_y]0.5r)T^{k+1}_{N_i-1,j+1} + (0.25q[u_x + u_y] + 0.5r)T^{k+1}_{N_i-1,j-1} \\ + \quad & (0.25q[-u_x + u_y] + 0.5r)T^{k+1}_{N_i+1,j-1} + (1 + 6r)T^{k+1}_{N_i,j} \ , \end{aligned} \tag{A.6}$$

and for $N_i + 1$, $T_{N_i+1,j} = T_{Hb}$,

$$
\begin{aligned}
T \;& {}^{k}_{N_i,j} - (u_x q - 2r)T_{Hb} + (0.25q[u_x + u_y] - 0.5r)T_{Hb} - (0.25q[-u_x + u_y] + 0.5r)T_{Hb} \\
= \;& -(u_x q + 2r)T^{k+1}_{N_i-1,j} + (u_y q - 2r)T^{k+1}_{N_i,j+1} - (u_y q + 2r)T^{k+1}_{N_i,j-1} \\
+ \;& (0.25q[u_x - u_y] + 0.5r)T^{k+1}_{N_i-1,j+1} + (0.25q[u_x + u_y] + 0.5r)T^{k+1}_{N_i-1,j-1} \\
+ \;& (1 + 6r)T^{k+1}_{N_i,j} \;, \qquad \text{(A.7)}
\end{aligned}
$$

and thus:

$$
\begin{aligned}
T^{k}_{N_i,j} + (-0.5u_x q + r)T_{Hb} \;& = \; -(u_x q + 2r)T^{k+1}_{N_i-1,j} + (u_y q - 2r)T^{k+1}_{N_i,j+1} \\
& - \; (u_y q + 2r)T^{k+1}_{N_i,j-1} + (0.25q[u_x - u_y] + 0.5r)T^{k+1}_{N_i-1,j+1} \\
& + \; (0.25q[u_x + u_y] + 0.5r)T^{k+1}_{N_i-1,j-1} + (1 + 6r)T^{k+1}_{N_i,j} \;. \qquad \text{(A.8)}
\end{aligned}
$$

At the boundary where $j = 1$ (assuming FD symmetry, i and j indices reversed; x and y too; and $T_{i,0} = T_{Hl}$),

$$
\begin{aligned}
T^{k}_{i,1} + (0.5qu_y + r)T_{Hl} \;& = \; (u_y q - 2r)T^{k+1}_{i,2} + (u_x q - 2r)T^{k+1}_{i+1,1} \\
& - \; (u_x q + 2r)T^{k+1}_{i-1,1} + (-0.25q[u_x + u_y] + 0.5r)T^{k+1}_{i+1,2} \\
& + \; (0.25q[u_x - u_y] + 0.5r)T^{k+1}_{i-1,2} + (1 + 6r)T^{k+1}_{i,1} \;. \qquad \text{(A.9)}
\end{aligned}
$$

At the boundary where $j = N_j$ (assuming $T_{i,N_j+1} = T_{Hr}$),

$$
\begin{aligned}
T^k_{i,N_j} + (-0.5u_y q + r)T_{Hr} &= -(u_y q + 2r)T^{k+1}_{i,N_j-1} + (u_x q - 2r)T^{k+1}_{i+1,N_j} \\
&- (u_x q + 2r)T^{k+1}_{i-1,N_j} + (0.25q[-u_x + u_y] + 0.5r)T^{k+1}_{i+1,N_j-1} \\
&+ (0.25q[u_x + u_y] + 0.5r)T^{k+1}_{i-1,N_j-1} + (1+6r)T^{k+1}_{i,N_j} \ . \quad \text{(A.10)}
\end{aligned}
$$

A.2 Adiabatic Boundaries

At the boundary where $j = 1$,

$$
\begin{aligned}
T^k_{i,1} &= (u_x q - 2r)T^{k+1}_{i+1,1} - (u_x q + 2r)T^{k+1}_{i-1,1} + (u_y q - 2r)T^{k+1}_{i,2} \\
&- (u_y q + 2r)T^{k+1}_{i,0} + (-0.25q[u_x + u_y] + 0.5r)T^{k+1}_{i+1,2} + (0.25q[u_x - u_y] + 0.5r)T^{k+1}_{i-1,2} \\
&+ (0.25q[u_x + u_y] + 0.5r)T^{k+1}_{i-1,0} + (0.25q[-u_x + u_y] + 0.5r)T^{k+1}_{i+1,0} \\
&+ (1+6r)T^{k+1}_{i,1} \ , \quad \text{(A.11)}
\end{aligned}
$$

and $T^{k+1}_{i,0} = T^{k+1}_{i,1}$, $T^{k+1}_{i+1,0} = T^{k+1}_{i+1,1}$, $T^{k+1}_{i-1,0} = T^{k+1}_{i-1,1}$, giving:

$$
\begin{aligned}
T^k_{i,1} &= (0.75qu_x + 0.25qu_y - 1.5r)T^{k+1}_{i+1,1} + (-0.75qu_x + 0.25qu_y - 1.5r)T^{k+1}_{i-1,1} \\
&+ (u_y q - 2r)T^{k+1}_{i,2} + (-0.25q[u_x + u_y] + 0.5r)T^{k+1}_{i+1,2} \\
&+ (0.25q[u_x - u_y] + 0.5r)T^{k+1}_{i-1,2} + (1 - u_y q + 4r)T^{k+1}_{i,1} \ . \quad \text{(A.12)}
\end{aligned}
$$

At the boundary where $j = N_j$,

$$
\begin{aligned}
T^k_{i,N_j} &= (u_x q - 2r)T^{k+1}_{i+1,N_j} - (u_x q + 2r)T^{k+1}_{i-1,N_j} + (u_y q - 2r)T^{k+1}_{i,N_j+1} \\
&- (u_y q + 2r)T^{k+1}_{i,N_j-1} + (-0.25q[u_x + u_y] + 0.5r)T^{k+1}_{i+1,N_j+1} \\
&+ (0.25q[u_x - u_y] + 0.5r)T^{k+1}_{i-1,N_j+1} + (0.25q[u_x + u_y] + 0.5r)T^{k+1}_{i-1,N_j-1} \\
&+ (0.25q[-u_x + u_y] + 0.5r)T^{k+1}_{i+1,N_j-1} + (1 + 6r)T^{k+1}_{i,N_j} \ , \qquad \text{(A.13)}
\end{aligned}
$$

and $T^{k+1}_{i,N_j+1} = T^{k+1}_{i,N_j}$, $T^{k+1}_{i+1,N_j+1} = T^{k+1}_{i+1,N_j}$, $T^{k+1}_{i-1,N_j+1} = T^{k+1}_{i-1,N_j}$, giving:

$$
\begin{aligned}
T^k_{i,N_j} &= (0.75qu_x + 0.25qu_y - 1.5r)T^{k+1}_{i+1,N_j} - (0.75qu_x + 0.25qu_y + 1.5r)T^{k+1}_{i-1,N_j} \\
&- (u_y q + 2r)T^{k+1}_{i,N_j-1} + (0.25q[u_x + u_y] + 0.5r)T^{k+1}_{i-1,N_j-1} \\
&+ (0.25q[-u_x + u_y] + 0.5r)T^{k+1}_{i+1,N_j-1} + (1 + u_y q + 4r)T^{k+1}_{i,N_j} \ . \qquad \text{(A.14)}
\end{aligned}
$$

At the boundary where $i = 1$, assuming FD symmetry, i and j indices reversed; x and y too, and $T^{k+1}_{0,j} = T^{k+1}_{1,j}$, $T^{k+1}_{0,j+1} = T^{k+1}_{1,j+1}$,$T^{k+1}_{0,j-1} = T^{k+1}_{1,j-1}$, giving:

$$
\begin{aligned}
T^k_{1,j} &= (0.75qu_y + 0.25qu_x - 1.5r)T^{k+1}_{1,j+1} + (-0.75qu_y + 0.25qu_x - 1.5r)T^{k+1}_{1,j-1} \\
&+ (u_x q - 2r)T^{k+1}_{2,j} + (-0.25q[u_x + u_y] + 0.5r)T^{k+1}_{2,j+1} \\
&+ (0.25q[-u_x + u_y] + 0.5r)T^{k+1}_{2,j-1} + (1 - u_x q + 4r)T^{k+1}_{1,j} \ . \qquad \text{(A.15)}
\end{aligned}
$$

At the boundary where $i = N_i$, $T^{k+1}_{N_i+1,j} = T^{k+1}_{N_i,j}$, $T^{k+1}_{N_i+1,j+1} = T^{k+1}_{N_i,j+1}$, $T^{k+1}_{N_i+1,j-1} = T^{k+1}_{N_i,j-1}$, giving:

$$
\begin{aligned}
T^k_{N_i,j} &= (0.75qu_y + 0.25qu_x - 1.5r)T^{k+1}_{N_i,j+1} - (0.75qu_y + 0.25qu_x + 1.5r)T^{k+1}_{N_i,j-1} \\
&- (u_x q + 2r)T^{k+1}_{N_i-1,j} + (0.25q[u_x + u_y] + 0.5r)T^{k+1}_{N_i-1,j-1} \\
&+ (0.25q[u_x - u_y] + 0.5r)T^{k+1}_{N_i-1,j+1} + (1 + u_x q + 4r)T^{k+1}_{N_i,j} \ . \qquad \text{(A.16)}
\end{aligned}
$$

A.3 Periodic Boundaries

Either add a new row of nodes to the outlet, which are not updated or write out the periodic boundary conditions.

$$
\begin{aligned}
T^k_{i,j} &= (u_x q - 2r)T^{k+1}_{i+1,j} - (u_x q + 2r)T^{k+1}_{i-1,j} + (u_y q - 2r)T^{k+1}_{i,j+1} \\
&- (u_y q + 2r)T^{k+1}_{i,j-1} + (-0.25q[u_x + u_y] + 0.5r)T^{k+1}_{i+1,j+1} \\
&+ (0.25q[u_x - u_y] + 0.5r)T^{k+1}_{i-1,j+1} + (0.25q[u_x + u_y] + 0.5r)T^{k+1}_{i-1,j-1} \\
&+ (0.25q[-u_x + u_y] + 0.5r)T^{k+1}_{i+1,j-1} + (1 + 6r)T^{k+1}_{i,j} \ . \qquad \text{(A.17)}
\end{aligned}
$$

At the boundary where $i = 1$,

$$
\begin{aligned}
T^k_{1,j} &= (u_x q - 2r)T^{k+1}_{2,j} - (u_x q + 2r)T^{k+1}_{0,j} + (u_y q - 2r)T^{k+1}_{1,j+1} \\
&- (u_y q + 2r)T^{k+1}_{1,j-1} + (-0.25q[u_x + u_y] + 0.5r)T^{k+1}_{2,j+1} \\
&+ (0.25q[u_x - u_y] + 0.5r)T^{k+1}_{0,j+1} + (0.25q[u_x + u_y] + 0.5r)T^{k+1}_{0,j-1} \\
&+ (0.25q[-u_x + u_y] + 0.5r)T^{k+1}_{2,j-1} + (1 + 6r)T^{k+1}_{1,j} \ , \qquad \text{(A.18)}
\end{aligned}
$$

and $T^{k+1}_{0,j} = T^{k+1}_{N_i,j}$, $T^{k+1}_{0,j+1} = T^{k+1}_{N_i,j+1}$, $T^{k+1}_{0,j-1} = T^{k+1}_{N_i,j-1}$, giving:

$$
\begin{aligned}
T^k_{1,j} &= (u_x q - 2r)T^{k+1}_{2,j} - (u_x q + 2r)T^{k+1}_{N_i,j} + (u_y q - 2r)T^{k+1}_{1,j+1} \\
&- (u_y q + 2r)T^{k+1}_{1,j-1} + (-0.25q[u_x + u_y] + 0.5r)T^{k+1}_{2,j+1} \\
&+ +(0.25q[u_x - u_y] + 0.5r)T^{k+1}_{N_i,j+1} + (0.25q[u_x + u_y] + 0.5r)T^{k+1}_{N_i,j-1} \\
&+ (0.25q[-u_x + u_y] + 0.5r)T^{k+1}_{2,j-1} + (1 + 6r)T^{k+1}_{1,j} \ . \qquad \text{(A.19)}
\end{aligned}
$$

At the boundary where $i = N_i$,

$$
\begin{aligned}
T^k_{N_i,j} &= (u_x q - 2r)T^{k+1}_{N_i+1,j} - (u_x q + 2r)T^{k+1}_{N_i-1,j} + (u_y q - 2r)T^{k+1}_{N_i,j+1} \\
&- (u_y q + 2r)T^{k+1}_{N_i,j-1} + (-0.25q[u_x + u_y] + 0.5r)T^{k+1}_{N_i+1,j+1} \\
&+ (0.25q[u_x - u_y] + 0.5r)T^{k+1}_{N_i-1,j+1} + (0.25q[u_x + u_y] + 0.5r)T^{k+1}_{N_i-1,j-1} \\
&+ (0.25q[-u_x + u_y] + 0.5r)T^{k+1}_{N_i+1,j-1} + (1 + 6r)T^{k+1}_{N_i,j} \ . \qquad \text{(A.20)}
\end{aligned}
$$

and $T^{k+1}_{N_i+1,j} = T^{k+1}_{1,j}$, $T^{k+1}_{N_i+1,j+1} = T^{k+1}_{1,j+1}$, $T^{k+1}_{N_i+1,j-1} = T^{k+1}_{1,j-1}$, giving:

$$
\begin{aligned}
T^k_{N_i,j} &= (u_x q - 2r)T^{k+1}_{1,j} - (u_x q + 2r)T^{k+1}_{N_i-1,j} + (u_y q - 2r)T^{k+1}_{N_i,j+1} \\
&- (u_y q + 2r)T^{k+1}_{N_i,j-1} + (-0.25q[u_x + u_y] + 0.5r)T^{k+1}_{1,j+1} \\
&+ (0.25q[u_x - u_y] + 0.5r)T^{k+1}_{N_i-1,j+1} + (0.25q[u_x + u_y] + 0.5r)T^{k+1}_{N_i-1,j-1} \\
&+ (0.25q[-u_x + u_y] + 0.5r)T^{k+1}_{1,j-1} + (1 + 6r)T^{k+1}_{N_i,j} \ . \qquad \text{(A.21)}
\end{aligned}
$$

At the boundary where $j = 1$, assuming FD symmetry, i and j indices reversed; x and y too, and $T^{k+1}_{i,0} = T^{k+1}_{i,N_j}$, $T^{k+1}_{i+1,0} = T^{k+1}_{i+1,N_j}$, $T^{k+1}_{i-1,0} = T^{k+1}_{i-1,N_j}$,

$$
\begin{aligned}
T^k_{i,1} &= (u_y q - 2r)T^{k+1}_{i,2} - (u_y q + 2r)T^{k+1}_{i,N_j} + (u_x q - 2r)T^{k+1}_{i+1,1} \\
&- (u_x q + 2r)T^{k+1}_{i-1,1} + (-0.25q[u_x + u_y] + 0.5r)T^{k+1}_{i+1,2} \\
&+ (0.25q[-u_x + u_y] + 0.5r)T^{k+1}_{i+1,N_j} + (0.25q[u_x + u_y] + 0.5r)T^{k+1}_{i-1,N_j} \\
&+ (0.25q[u_x - u_y] + 0.5r)T^{k+1}_{i-1,2} + (1 + 6r)T^{k+1}_{i,1} \ . \qquad \text{(A.22)}
\end{aligned}
$$

At the boundary where $j = N_j$, assuming FD symmetry, i and j indices reversed; x and y too, and $T^{k+1}_{N_i+1,j} = T^{k+1}_{1,j}$, $T^{k+1}_{N_i+1,j+1} = T^{k+1}_{1,j+1}$, $T^{k+1}_{N_i+1,j-1} = T^{k+1}_{1,j-1}$,

$$
\begin{aligned}
T^k_{i,N_j} &= (u_y q - 2r)T^{k+1}_{j,1} - (u_y q + 2r)T^{k+1}_{i,N_j-1} + (u_x q - 2r)T^{k+1}_{i+1,N_j} \\
&- (u_x q + 2r)T^{k+1}_{i-1,N_j} + (-0.25q[u_x + u_y] + 0.5r)T^{k+1}_{i+1,1} \\
&+ (0.25q[-u_x + u_y] + 0.5r)T^{k+1}_{i+1,N_j-1} + (0.25q[u_x + u_y] + 0.5r)T^{k+1}_{i-1,N_j-1} \\
&+ (0.25q[u_x - u_y] + 0.5r)T^{k+1}_{i-1,1} + (1 + 6r)T^{k+1}_{i,N_j} \ . \qquad \text{(A.23)}
\end{aligned}
$$

APPENDIX B

ORGANIC ACID REACTIONS

B.1 Carbonate Reactions with Organic Acid: Rate and Temperature Changes

The molarities for a 13% acetic acid solution and a 9% formic acid solution are 2.167 mol/liter and 2.83 mol/liter, respectively. At room temperature the dissociation constants for acetic and formic acids are 1.8×10^{-5} and 1.8×10^{-4}, respectively (Buijse et al., 2004). Buijse et al. suggest that given a 13% acetic acid, 9% formic acid solution that the concentration of the acids after reaction with carbonate rock would be 31% and 82%, respectively. This would be expected as the reaction caused by weaker component of the acid mixture is usually suppressed. Other models have been summarized in Li et al. (2008). The pK_a value for formic acid can be described by the following correlation (Kim et al., 1996):

$$pK_a = -57.528 + 2773.9/T + 9.1232ln(T) \ , \tag{B.1}$$

and is shown in **Fig. (B.1)**.

The remaining spent acid concentration can then be determined using Eq. (B.2) (Buijse et al., 2004)):

$$[HA]_s = \frac{[H^+]_s \left([H^+]_s + K_a\right)}{K_a} \tag{B.2}$$

As the temperature increases, the degree of hydrogen ion generation decreases. Therefore, the pK_a value increases resulting in a decrease in the amount of spent acid. At 100^oC the value for pK_a increases to 3.93 for formic acid.

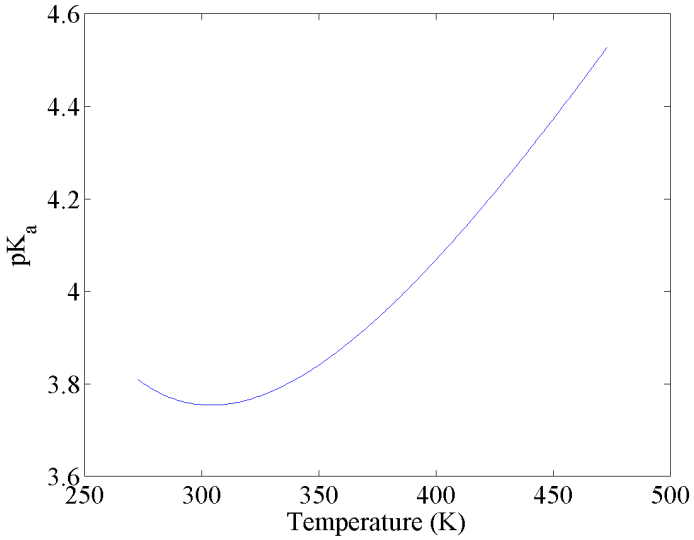

Figure B.1: The pK$_a$ value for formic acid as a function of temperature.

APPENDIX C

CHOICE OF DAMKÖHLER NUMBER

Damköhler numbers of the first and second kind take the form (Lichtner and Kang, 2007):

$$Da_I = \frac{\tilde{k}\tilde{\delta}l}{\tilde{\mathcal{D}}} = \frac{k\delta l}{\mathcal{D}} \,, \tag{C.1}$$

and

$$Da_{II} = \frac{\tilde{k}}{\tilde{u}} = \frac{k}{u} \,. \tag{C.2}$$

Table C.1: Parameters used by Kang et al. (2002).

Type of Acid	$\mathcal{D}_R$ ($m^2\ s^{-1}$)	k_r ($m\ s^{-1}$)	K_{eq}
0.5M HCl	3.6×10^{-9}	2×10^{-3}	1×10^{10}

Considering a sample of size $0.486 \times 0.586 \times 0.586$ mm, the Damköhler numbers are then:

$$Da_I = \frac{(2 \times 10^{-3})(5.4 \times 10^{-6})}{3.6 \times 10^{-9}} = 3 \,, \tag{C.3}$$

and

$$Da_{II} = \frac{2 \times 10^{-3}}{6.4 \times 10^{-3}} = 0.31 \,. \tag{C.4}$$

Eq. (C.4) is approximately the optimal Damköhler number reported by Fredd and Fogler (1998). The lattice reaction rate is therefore:

$$\tilde{k}_r = \tilde{u}\, Da_{II} = (0.0058)(0.31) = 1.8 \times 10^{-3} \text{ lu lt}^{-1} \; . \tag{C.5}$$

Alternatively, Kang and Lichtner (2007) describe the Damköhler number as:

$$Da = \frac{k_r b}{\mathcal{D}} \; , \tag{C.6}$$

where b is the characteristic height of the domain. They performed a simulation for advection, diffusion, and reaction in an open channel of dimension 400×64 LUS or 5×0.75 cm and at $Da = 7.5 \times 10^{-2}$. The following lattice parameters were given:

Table C.2: Parameters used by Kang and Lichtner (2007).

Average Velocity, u_{av}	Diffusivity, $\mathcal{D}$	Reaction Rate, k_r	Equilibrium Constant, K_{eq}
0.05	0.25	3.125×10^{-4}	10

In order to recover the above Damköhler number, the following form must be used:

$$Da = \frac{k_r b}{\mathcal{D}} = \frac{(3.125 \times 10^{-4})(60)}{0.25} = 7.5 \times 10^{-2} \; . \tag{C.7}$$

If, however, this form is used to reproduce the results of Kang et al. (2002), the Damköhler number would be:

$$Da = \frac{k_r b}{\mathcal{D}} = \frac{(2 \times 10^{-3})(5.86 \times 10^{-4})}{3.6 \times 10^{-9}} = 325.6 \; . \tag{C.8}$$

Based on this description, the lattice reaction rate would be:

$$\tilde{k}_r = \frac{\tilde{\mathcal{D}}\, Da}{b} = \frac{1}{6}\frac{325.6}{106} = 0.51 \text{ lu lt}^{-1} \ . \tag{C.9}$$

Based on the optimal Damköhler number found by Fredd and Fogler (1998), Eq. (C.4) would be assumed to be most accurate. However, throughout their work, Kang et al. reference Eq. (C.6) and this convention is followed here.